Organization and diffusion in biological and material fabrication problems

Organization and diffusion in biological and material fabrication problems

a dissertation presented
by
Niall Mari Mangan
to
The Committee on Higher Degrees in Systems Biology

in partial fulfillment of the requirements
for the degree of
Doctor of Philosophy
in the subject of
Systems Biology

Harvard University
Cambridge, Massachusetts
June 2013

Thesis advisor: Michael Brenner Niall Mari Mangan

Organization and diffusion in biological and material fabrication problems

Abstract

This thesis is composed of two problems. The first is a systems level analysis of the carbon concentrating mechanism in cyanobacteria. The second presents a theoretical analysis of femtosecond laser melting for the purpose of hyperdoping silicon with sulfur. While these systems are very distant, they are both relevant to the development of alternative energy (production of biofuels and methods for fabricating photovoltaics respectively). Both problems are approached through analysis of the underlying diffusion equations.

Cyanobacteria are photosynthetic bacteria with a unique carbon concentrating mechanism (CCM) which enhances carbon fixation. A greater understanding of this mechanism would offer new insights into the basic biology and methods for bioengineering more efficient biochemical reactions. The molecular components of the CCM have been well characterized in the last decade, with genetic analysis uncovering both variation and commonalities in CCMs across cyanobacteria strains. Analysis of CCMs on a systems level, however, is based on models formulated prior to the molecular characterization. We present an updated model of the cyanobacteria CCM, and analytic solutions in terms of the various molecular components. The solutions allow us to find the parameter regime (expression levels, catalytic rates, permeability of carboxysome shell) where carbon fixation is maximized and oxygenation is minimized.

Saturation of RuBisCO, maximization of the ratio of CO_2 to O_2 , and staying below or at the saturation level for carbonic anhydrase are all needed for maximum efficacy. These constraints limit the parameter regime where the most effective carbon fixation can occur. There is an optimal non-specific carboxysome shell permeability, where trapping of CO_2 is maximized, but HCO_3^- is not detrimentally restricted. The shell also shields carbonic anhydrase activity and $CO_2 \rightarrow HCO_3^-$ conversion at the thylakoid and cell membrane from one another. Co-localization of carbonic anhydrase and RuBisCO in a smaller volume raises the concentration of carbon dioxide around RuBisCO by switching from a regime where the carbonic anhydrase is saturated to non-saturated.

Hyper-doping with femto-second lasers offers a versatile method for creating new materials including semi-conductor materials doped at beyond the equilibrium solubility limit. Silicon hyper-doped with sulfur has been shown to absorb highly in the infra-red region. Hyper-doped silicon already is already used in night-vision infra-red sensors and is being explored for other applications such as photovoltaics. Being able to finely tune the dopant profile in the material will allow us to achieve more efficient and effective devices. To better control the doping profile, we develop a model which correctly represents the physics of melting of Si and diffusion of dopant into the material. The thermal and solute diffusion model produces melt dynamics and dopant profiles consistent with experimental data. We present the results of numerical simulations. We identify two distinct mechanisms which account for the characteristic dopant profiles in experiments. A change in laser absorption such that the melt depth increases or a

change in the mechanism of dopant integration from an ”instant surface dose” to a surface flux can both account for changes in dopant profile with subsequent laser pulses.

Contents

Listing of figures

For my family.

Acknowledgments

I would like to thank everyone who has helped me in the last five years. I am grateful to my colleagues, collaborators, friends and family who have supported me.

I am grateful to my advisor Michael Brenner for guiding me through the graduate school experience. Michael taught me how to balance what is important and leave the rest. Thank you, Michael, for your patience, enthusiasm, and pragmatism. The answer is what it is, and it is exciting.

I would like to thank all the members of the Brenner group for discussions, lunches, and constructive criticism. Joerg Fritz, thank you for sharing the experience as officemate and friend. Shreyas Mandre, thank you for your advice and friendship. Thanks to Sophie Marbach for enthusiastically getting involved in the fs-laser project and making last minute figures. Tobias Schneider created the numerical simulation for the femtosecond laser project. Agnese Seminara, Arvind Murugan, Karen Alim, Mark Henle, thank you for many the conference or luncheon discussion about science and life.

I am thankful for being a part of the collaborative Black Si community. Thanks again to Michael for remembering I was interested in solar energy outside of photosynthesis and giving me the opportunity and freedom to work on such a project. Renee Sher and Yu-Ting Lin, thank you for entertaining my often nutty theories. I am grateful to Dan Rect, Jacob Krich, Mike Aziz, Eric Mazur and the

rest of the black silicon community for discussion and feedback.

I am grateful to Pam Silver for allowing me in and out of her lab sporadically. Thank you to Michael Moore and Dan Savage for mentoring in experiments during my time in lab. Anna Chen, Bruno Afanso, Gairik Sachdeva, Danny Ducat, Patrick Boyle and the rest of the Silver Lab were indispensable for discussions on carboxysomes, cyanobacteria and alternative energy.

I am indebted to Colleen Cavanaugh, Pam Silver and Jeremy Gunawardena for an incredibly pleasant and productive advisory committee experience over the last four years. Thank you to Katia Bertoldi for joining my defense committee.

Thank you to my friends, roommates, and family for incredible support. I feel lucky to have been part of a systems biology cohort who are not only great scientists but a community. Thank you, John, Ani and Brad for being an awesome household. Jessie, thank you for being there when I needed someone to talk to. James, thank you and much love. A big thank you to my parents for all the love and the weekly phone calls spattered with advice and understanding.

Acknowledgment of Funding:

This research was funded by an NSF graduate fellowship, and a Lynch Fellowship.

1

Systems analysis of the carbon concentrating mechanism in cyanobacteria

1.1 Introduction

Cyanobacteria are of interest as model organisms for photosynthesis as well as a chassis for synthesis of products including biofuels [44, 45]. Strikingly the principal reaction of the Calvin cycle, the RuBisCO catalyzed fixation of CO_2 into 3-phosphoglycerate, occurs in small, 500nm, compartments called carboxysomes [11, 67]. There is much interest in the function of these compartments and whether they can be used to enhance reaction rates in other metabolic systems [9, 18, 34].

The carbon concentrating mechanism, Fig 1.1.1 can raise internal inorganic carbon concentration to around 15 mM, up to 4,000-fold higher than external levels [55, 64], allowing the cell to overcome the slow and oxygen sensitive RuBisCO [57] . A much lower CO_2 concentration, around 250 μM, saturates the 2160 active sites of RuBisCO found in a carboxysome; thus the extra CO_2 cannot improve the rate of sugar production by providing more substrate for fixation. RuBisCO competitively binds with both CO_2 and oxygen, and the reaction with oxygen produces phosphoglycolate, a waste product which must be recycled by the cell [23, 46, 57]. By elevating the concentration of CO_2 the ratio of CO_2 to oxygen is increased, and the CO_2 reaction dominates.

The concentrating mechanism in cyanobacteria relies on the interaction of a number of well characterized components, transferring carbon pools outside the cell into carboxysomes [1, 4, 24, 38] . RuBisCO can only utilize CO_2 for carboxylation, however the bilipid cell membrane is highly permeable to small uncharged molecules, making it difficult to accumulate a large pool of CO_2 [19, 32]. To circumvent this, the cell accumulates the hydrated form HCO_3^-, which is much less membrane soluble, owing to its electrostatic charge. The bicarbonate is then converted to CO_2 near RuBisCO by the enzyme carbonic anhydrase, which is localized on the interior side of the carboxysome shell [10, 14, 29, 67]. The relative proportion of HCO_3^- and CO_2 in equilibrium are pH dependent. However, experiments expressing exogenous carbonic anhydrase inside the cytoplasm showed an enormous efflux of carbon dioxide from cells, indicating that bicarbonate is held out of chemical equilibrium in high concentration [40]. A variety of active transporters, both constitutive and inducible, bring HCO_3^- into the cell [33, 37, 39]. There are also mechanisms, referred to as facilitated CO_2 uptake mechanisms or CO_2 scavenging mechanisms, which actively convert CO_2 to HCO_3^- at the thylakoid and cell membrane [13, 31, 39]. Time course measurements of external carbon dioxide changes using a mass spectrometer have measured external or aggregate carbon fluxes [55, 64]. Since HCO_3^- is held out of equilibrium in the cell [40], its conversion to CO_2 in the carboxysome results in local production of CO_2 near

RuBisCO. Subsequently, RuBisCO catalyzes the reaction of carbon dioxide with ribulose-1,5-bisphosphate to produce 3-phosphoglyceric acid. When the carbonic anhydrase associated with the carboxysome was knocked out or the carboxysomes are knocked out or broken, cells need high carbon dioxide levels to grow [17].

The function of the system and its ability to concentrate carbon depend on the interplay between the various molecular components that make up the carbon concentrating mechanism: the rates of bicarbonate transporters, the carbonic anydrase activity, the function and effect of the carboxysome shell, and the enzymatic conversion of CO_2 to HCO_3^- all influence the carbon concentrating mechanism. From flux measurements alone, it is impossible to determine the relative roles of these different components and interpretations rely on a model. To date, it has not been possible to directly measure the concentration of the internal carbon pool in the carboxysomes from the cytosol. For these reasons, the precise function and effect of the various components is still debated. Visualizations of the location of the carboxysomes shell and RuBisCO with florescent proteins in *S. elongatus* PCC7942 demonstrated that the carboxysomes are located along the centerline of the cell, and are held rigidly separated from one another at a spacing which scales with the length of the cell [45]. Given the importance of these compartments for carbon fixation, we investigate whether the spatial organization of the carboxysomes within the cell affects their function in the carbon concentrating mechanism.

The goal of this chapter is to develop a mathematical model of the carbon concentrating mechanism that allows predicting the region of parameter space where carbon fixation is efficient. Efficient carbon fixation requires two main ingredients: First, the internal carbon concentration must be high enough that Rubisco is saturated, and the competitive reaction with O_2 is negligible; Secondly, the carbonic anhydrase within the carboxysome must be unsaturated, so that extra energy isn't wasted transporting unused HCO_3^- into the cell. Examining the performance of the system with respect to the expression levels of

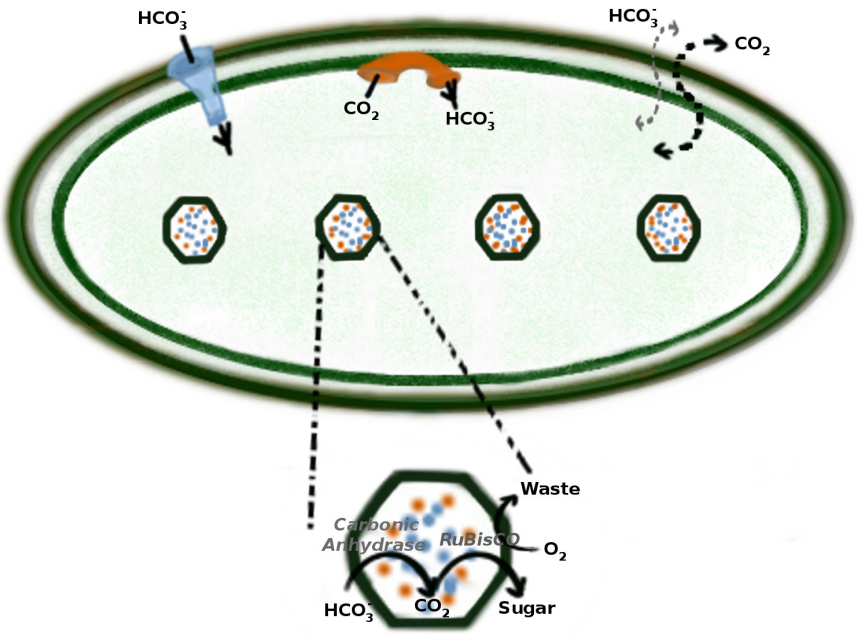

Figure 1.1.1: Schematic of the carbon concentrating mechanism in cyanobacteria. Cell membranes are the outer most membrane (in green/black). Immediately inside are the thylakoid membranes where the light reactions take place (in green). Carboxysomes are shown as four hexagons evenly spaced along the centerline of the cell. HCO_3^- transport across the cell membrane is indicated (in blue), as well as conversion from CO_2 to HCO_3^- (in orange). Both carbon species can leak in and out of the cell. Carbonic anhydrase (orange) and RuBisCO (blue) are confined to the carboxysomes and facilitate reactions as shown.

HCO_3^- transporters, the carboxysome permeability, and conversion from CO_2 to HCO_3^-, reveals a region of parameter space where both of these conditions are satisfied. Previous mathematical models have represented the effects of carbon fixation for only a single set of parameters, which is less useful since many of the parameters are either unknown (i.e. carboxysome permeability), or under physiological control (i.e. number of active HCO_3^- transporters) [5, 41, 43].

Having found the parameter space where carbon fixation will be optimal, we

can comment on the relation of this space to measured carbon pools. We also discuss the how much of the carbon concentration comes from different methods of spatial organization such as co-localization, encapsulation, and spatial location of carboxysomes.

1.2 Reaction diffusion model

Our model of the carbon concentrating mechanism solves for both the HCO_3^-, and CO_2, concentration throughout the cell and the carboxysome. We include the effects of diffusion, active transport and leakage through the cell membrane, and reactions with carbonic anhydrase and RuBisCO. The hydration and dehydration of CO_2 and HCO_3^- without enzymatic activity are comparatively processes and can be safely ignored.

In regions with carbonic anhydrase activity, the equations governing the HCO_3^-, H, and CO_2, C, are

$$\partial_t C = D\nabla^2 C + R_{CA} - R_{Rub} \tag{1.1}$$

$$\partial_t H = D\nabla^2 H - R_{CA}, \tag{1.2}$$

where here D is the diffusion constant, and R_{CA} is the carbonic anhydrase reaction, and R_{Rub} is the RuBisCO reaction. The carbonic anhydrase reactions can be written using reversible Michaelis-Menten kinetics [24, 38],

$$R_{CA}(H, C) = \frac{V_{ba}K_{ca}H - V_{ca}K_{ba}C}{K_{ba}K_{ca} + K_{ca}H + K_{ba}C} \tag{1.3}$$

Here V_{ca} and V_{ba} are the maximum hydration and dehydration rates, and K_{ca} and K_{ba} are the concentration at which hydration and dehydration are half maximum. In regions of the cell where there is no carbonic anhydrase, $R_{CA} = 0$ and there is only diffusion of CO_2 and HCO_3^-.

The RuBisCO reaction can be described using Michaelis-Menten kinetics

with competitive binding with O_2, O.

$$R_{Rub} = \frac{V_{max} C}{C + K_m} \tag{1.4}$$

$$K_m = K'_m(1 + \frac{O}{K_i}) \tag{1.5}$$

Here V_{max} is the maximum rate of carbon fixation by RuBisCO and K_m is the apparent half maximum concentration value, which has been modified to include competitive binding with O_2. K_i is the disassociation constant of O_2 with the RuBisCO and K'_m is the half maximum concentration with no O_2 present.

We must supplement the equations with boundary conditions, which treat the carbon fluxes into the cell, as well as the transfer across the carboxysome boundary. For the outer boundary, we treat the carbon fluxes at cell and thylakoid membranes together. There are multiple active HCO_3^- transporters. BCT1 is thought to be energized by ATP, SbtA is thought to be a symporter between HCO_3^- and Na+, which is driven by the highly controlled electrochemical gradient for Na+ [33, 37, 39]. We can write the total flux velocity, j_c, as a combination of the flux from all types of transporters $j_c = j_{BCT1} + j_{SbtA}$. There are two complexes NDH-1_3 and NDH-1_4 responsible for converting CO_2 to HCO_3^- . They are thought to be localized to the thylakoid and plasma membrane respectively and have been linked to the photosynthetic linear and cyclic electron chain [13, 31, 39]. We can describe their activity with a maximal reaction rate of a, and concentration of half maximal activity of K_a. In addition to active processes at the cell membrane, CO_2 and HCO_3^- can both leak out. The velocity of CO_2 crossing the cell membrane, k_m^C, is about 1000 fold lower than that for HCO_3^-, k_m^H, due to the lower permeability of the membrane to charged molecules. These components define the boundary condition for bicarbonate and carbon dioxide at the cell membrane:

$$D\frac{\partial C}{\partial r} = -\frac{a C_{cytosol}}{K_a + C_{cytosol}} + k_m^C \left(C_{out} - C_{cytosol}\right) \tag{1.6}$$

$$D\frac{\partial H}{\partial r} = j_c H_{out} + \frac{aC_{cytosol}}{K_a + C_{cytosol}} + k_m^H \left(H_{out} - H_{cytosol}\right) \tag{1.7}$$

Here the subscript *cytosol* and *out* indicate we are taking the concentration immediately inside and outside the cell membrane respectively.

Unlike the outer cell membrane, which is a lipid bilayer, the carboxysome shell is a composed of proteins. The structure of the carboxysome has been characterized through crystallization experiments [12, 66, 67]. While there is much speculation that the positively charged pores may act selectively towards molecules with negative charge [12, 17, 67], we will assume a single permeability for all small molecules. We describe the rate of restricted diffusion across the carboxysome shell by a characteristic velocity, k_c. From available crystal structures we can set an upper bound on this value as

$$k_c < \frac{DA_{pore}}{lS_{carboxysome}}(N_{pores}) \approx 0.02\frac{cm}{s} \tag{1.8}$$

Here, D is the diffusion constant, A_{pore} is the surface area of a pore, l is the thickness of the carboxysome shell or length of a pore, $S_{carboxysome}$ is the surface area of a carboxysome, and N_{pores} is the number of pores in a carboxysome. These parameters have been found from the crystallization experiments and theoretical carboxysome structures, and their values are shown in Table 1.2.1.

The boundary conditions that connect the equations in the cytosol and carboxysome are:

$$D\frac{\partial C}{\partial r} = k_c(C_{cytosol} - C_{carboxysome}) \tag{1.9}$$

$$D\frac{\partial H}{\partial r} = k_c(H_{cytosol} - H_{carboxysome}). \tag{1.10}$$

The subscripts *cytosol* and *carboxysome* indicate we are taking the

Table 1.2.1: Carboxysome shell geometry, used to calculate a carboxysome permeability [59, 66].

	symbol	value
diameter of pore	d_{pore}	$0.7\ nm$
area of pore	$A_{pore} = \pi(\frac{d_{pore}}{2})^2$	$0.3\ nm^2$
thickness of shell	l	1.8 nm
number of pores	N_{pores}	4, 800
radius of carboxysome	R_c	500 nm
surface area of carboxysome	$S_{carboxysome} = 4\pi R_c^2$	$3.14 \times 10^6\ nm^2$

concentration immediately on either side of the carboxysome shell. This description allows us to determine how the permeability, characterized by velocity k_c, affects the CCM without any special selectivity.

1.3 Analysis of model: Finding functional parameter space

We need to solve these equations as a function of the parameters, to find the regime where efficient carbon fixation occurs. We find the functional relationship between the CO_2 and HCO_3^- concentration, and all components of the carbon concentrating mechanism at steady state. We analyze this system in spherical coordinates, assuming a spherical cell of radius, R_b and a single spherical carboxysome with radius R_c containing RuBisCO and carbonic anhydrase. We numerically and analytically solve equations (1.1) through (1.10) at steady state in the geometry described above. We focus on the HCO_3^- transport, carboxysome permeability, and CO_2 scavenging or facilitated uptake:

$$C_{carboxysome} = F(j_c, k_c, a, K_a). \tag{1.11}$$

All plots are shown with other parameters, including enzymatic rates, cell membrane permeability, and diffusion constant, treated as constant. We have analytic solutions for all behaviors, so we could also explore how changing these

values changes the behavior. However, HCO_3^- transport and CO_2 to HCO_3^- conversion are regulated by the organism and vary depending on environmental conditions. Carboxysome permeability is unknown, and there is much discussion about its potential value and benefits. We have therefore chosen these as the most interesting parameters to explore.

We first define the range of values for HCO_3^- transport, j_c, carboxysome permeability, k_c, where the carbon concentrating mechanism is most effective. The resulting CO_2 level in the carboxysome should be above RuBisCO saturation levels, high enough to reduce the O_2 side reactions as much as possible. We can set an upper bound on the concentration of HCO_3, as the level at which it will saturate carbonic anhydrase. When carbonic anhydrase is saturated, it cannot produce CO_2 faster than the constant maximum rate, and any excess energy spent bringing HCO_3^- into the cell is wasted. The range of HCO_3^- transport and carboxysome permeability which will produce HCO_3^- and CO_2 concentrations between these constraints shown in Fig. 1.3.1. We will later explore the effects of CO_2 to HCO_3^- conversion.

We will now examine one parameter at a time to show how the parameter ranges shown in Fig. 1.3.1 are found. We observe how the concentration of CO_2 and HCO_3^- in the carboxysome change as the HCO_3^- transport varies. Varying HCO_3^- transport, j_c, effectively probes the response of the rest of the carbon concentrating mechanism to varying amounts of HCO_3^- when active HCO_3^- uptake is the main souce of inorganic carbon. The system has varying responses as the level of inorganic carbon saturates RuBisCO and carbonic anhydrase. Fig. 1.3.2 shows the behaviors of the CO_2 and HCO_3^- concentration. At relatively low levels of HCO_3^- transport, CO_2 and HCO_3^- have a constant ratio, set by the chemical equilibrium. At higher levels, carbonic anhydrase is saturated, CO_2 no longer increases, and HCO_3^- continues to increase linearly with increasing j_c. We determine the analytic solutions below and above carbonic anhydrase saturation, and then set the analytic solutions equal to the desired carbon concentration for

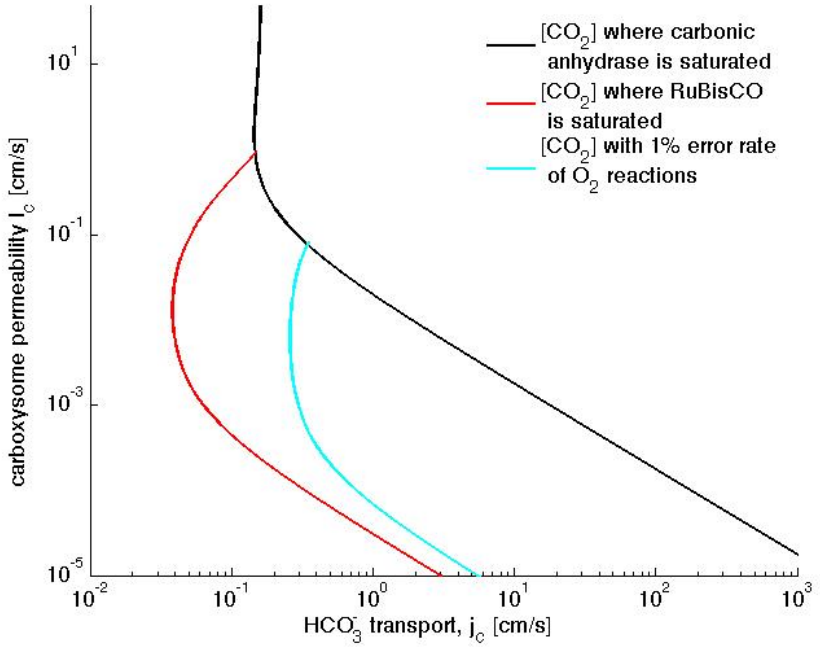

Figure 1.3.1: Phase space for HCO_3^- transport and carboxysome permeability. Plotted are the parameter values at which the CO_2 concentration reaches some critical value. The red line (left most) indicates for what values of j_c and k_c the CO_2 concentration in the carboxysome would saturate RuBisCO. The black line (right most) indicates the parameters for which carbonic anhydrase is saturated. The blue line (middle) indicates the parameter values which would result in a CO_2 concentration where 99% of all RuBisCO reactions are carboxylation reactions and only 1% are oxygenation reactions when O_2 concentration is $260\mu M$. Here $a = 0$, so there is no CO_2 scavenging or facilitated uptake. All other parameters, such as reaction rates are held fixed and the value can be found in tables A.0.1 and A.0.2.

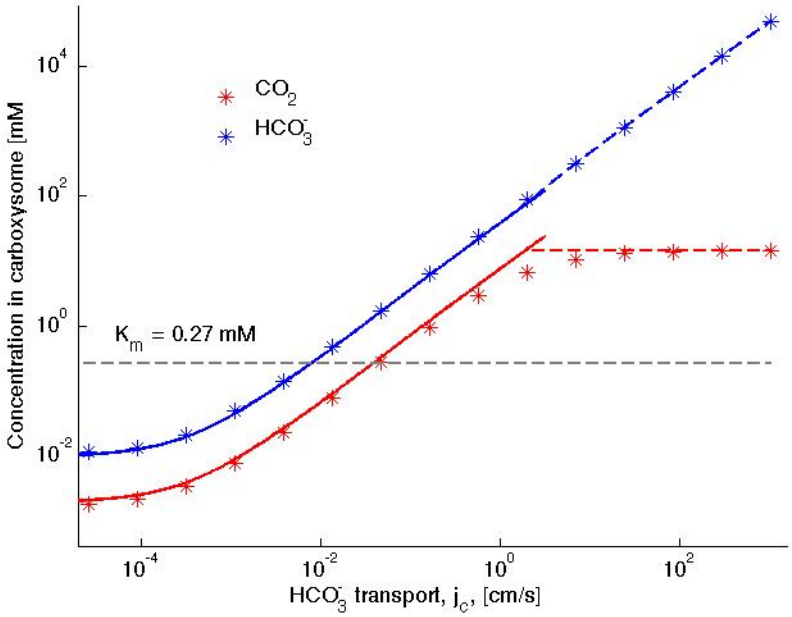

Figure 1.3.2: Numerical solutions (stars) compared to the solutions set by equation(1.12) (dashed line) and equations (1.21) and (1.22) (solid line). $\mathrm{HCO_3^-}$ transport is varied, and all other system parameters are held constant. The grey dashed line show the $\mathrm{CO_2}$ concentration at which RuBisCO is saturated, K_{max}. Below a critical value of transport, $j_c \approx 1e^{-3}$ the level of transport is lower than the $\mathrm{HCO_3^-}$ leaking through the cell membrane.

an effective carbon concentrating mechanism.

1.3.1 Carbonic anhydrase equilibrates CO_2 and HCO_3^-

To describe the behavior below a critical j_c threshold (about $j_c \approx 0.1$ in Fig 1.3.2), we need to find the appropriate solutions for CO_2 and HCO_3^- concentration in the carboxysome and in the cytosol, couple them together with the boundary condition at the carboxysome, and enforce the boundary conditions at the cell membrane.

When carbonic anhydrase equilibrates HCO_3^- and CO_2, diffusion within the carboxysome is negligible and the solution is set by $R_{CA} = \frac{V_{ba}K_{ca}H - V_{ca}K_{ba}C}{K_{ba}K_{ca} + K_{ca}H + K_{ba}C} = 0$, indicating:

$$H = \frac{V_{ca}K_{ba}}{V_{ba}K_{ca}}C. \tag{1.12}$$

Note that the time scale associated with diffusion for a small molecule across a 100 nm carboxysome is about the same as the timescale for highly concentrated carbonic anhydrase. There is a very small gradient across the carboxysome and the size of this gradient gives us the error in our approximation.

The chemical equilibrium for carbonic anhydrase is set by the Haldane relation, $K_{eq} = \frac{K_{ba}V_{ca}}{K_{ca}V_{ba}} = \frac{[CO_2]}{[HCO_3^-][H^+]}$, and varies with pH [16]. For the pH range between 7 and 8, measured values of these parameters give an estimate of $K_{eq} \approx 5$ [20]. Since $K_{eq} > 1$, then the back reaction will be favored, producing a smaller amount of CO_2 in the carboxysome than if the forward reaction were favored.

We need to couple the behavior in the carboxysome to the behavior in the cytosol, where there is no carbonic anhydrase and only diffusion. In spherical coordinates the solutions to $\nabla^2 C = 0$ and $\nabla^2 H = 0$ have the form

$$C = \frac{A_3}{r} + A_4 \tag{1.13}$$

$$H = \frac{B_3}{r} + B_4 \tag{1.14}$$

where the boundary conditions at the cell membrane, equations (1.6) and (1.7) set two of the constants, A_3, A_4, B_3, and B_4. The two others are set by the boundary condition at the carboxysome, equations (1.9) and (1.10).

Increasing HCO_3^- beyond the carbonic anhydrase saturation point confers no added benefit. Therefore, in the interesting regime CO_2 and HCO_3^- are set by equation (1.12) where carbonic anhydrase equilibrates the carbon concentrations in the carboxysome.

The total carbon flux in and out of the carboxysome must be equal to the consumption of CO_2 by RuBisCO.

$$\int D\frac{\partial(C+H)}{\partial r}(r=R_c)dS_{carboxysome} = \int \frac{V_{max}C_{carboxysome}}{C_{carboxysome}+K_m}dV_{carboxysome} \tag{1.15}$$

We can exactly solve this equation for the concentration in CO_2, since it is just a quadratic equation. For the benefit of the reader we constrain these ungainly equations to the appendix. Given measured carbon pools would saturate RuBisCO, we are most interested interested in the solution when RuBisCO is saturated. Using the RuBisCO saturated limit of equation (1.15), the solutions in the cytosol: equations (1.13) and (1.14), the boundary conditions at the carboxysome: equations (1.9) and (1.10), and the boundary conditions at the cell membrane: equations (1.6) and (1.7), the CO_2 concentration in the cell and carboxysome is:

$$C_{cytosol} = \frac{k_m^C C_{out} - (k_m^C + \frac{a}{K_a}) C_{carboxysome}}{(\frac{a}{K_a} + k_m^C) G + \frac{D}{R_b^2}} \left(\frac{D}{R_c^2 k_c} + \frac{1}{R_c} - \frac{1}{r} \right) + C_{carboxysome} \tag{1.16}$$

$$C_{carboxysome} = \frac{(j_c + k_m^H)((k_m^C + \frac{a}{K_a})G + \frac{D}{R_b^2}) H_{out} + k_m^C((k_m^H + \frac{a}{K_a})G + \frac{D}{R_b^2}) C_{out}}{(k_m^C + \frac{a}{K_a}) k_m^H (1 + \frac{K_{ba} V_{ca}}{K_{ca} V_{ba}}) G + \left(1 + \frac{k_m^H}{k_m^c} \frac{K_{ba} V_{ca}}{K_{ca} V_{ba}}\right) k_m^C \frac{D}{R_b^2}} - \frac{R_c^3 V_{max} ((\frac{a}{K_a} + k_m^C) G + \frac{D}{R_b^2}) (k_m^H G + \frac{D}{R_b^2})}{3D((k_m^C + \frac{a}{K_a})(1 + \frac{V_{ca} K_{ba}}{V_{ba} K_{ca}}) k_m^H G + k_m^C (1 + \frac{k_m^H}{k_m^C} \frac{V_{ca} K_{ba}}{V_{ba} K_{ca}}) \frac{D}{R_b^2})} \tag{1.17}$$

where

$$G = \left(\frac{D}{R_c^2 k_c} + \frac{1}{R_c} - \frac{1}{R_b} \right). \tag{1.18}$$

These equations determine the CO_2 concentration in the cell and carboxysome when RuBisCO is saturated but carbonic anhydrase is not.

To find the values of HCO_3^- transport, j_c, and carboxysome permeability, k_c, which will result in RuBisCO saturation, we set the solution found without assuming RuBisCO saturation (Appendix equation (A.55)) equal to $C_{carboxysome} = K_m$. The resulting equation gives a relationship between j_c and k_c, the red line in Fig. 1.3.1. To the left of this line, RuBisCO is unsaturated. To the right of the line RuBisCO is saturated and equation (1.17) holds until carbonic anhydrase becomes saturated.

For the blue curve we determine the relationship between k_c and j_c values by setting equation (1.17) equal to the CO_2 concentration which will result in the desired rate of oxygenation reactions. To find the CO_2 concentrations where 99% of reactions are carboxylations we calculate the ratio of carboxylation to oxygenation reactions, when RuBisCO is saturated, as follows:

$$\frac{carboxylation\ rate}{oxygenation\ rate} = \frac{V_{max}}{V_O} \frac{C}{O} = 99 \tag{1.19}$$

$$C_{99\%} = 99\ O\ \frac{V_O}{V_C} \approx 2mM \tag{1.20}$$

where V_O, is the maximum rate of RuBisCO oxygenation, and O is the concentration of O_2. In Fig. 1.3.1, the region to the left the blue line representing 1% oxygenation error rate, will have an error rate below 1%.

Both the $CO_2 = C_{99\%}$, and $CO_2 = K_m$ lines are constant concentration lines in j_c and k_c parameter space. The plot shows that varying carboxysome permeability, k_c values, require more or less HCO_3 transport, j_c, to achieve the same carbon concentration. At high and low k_c a higher j_c is required, and there is a particular value $k_c \approx 1e^{-5}\frac{cm}{s}$ for which the least j_c is needed. At very low, restrictive values of k_c, HCO_3^- diffuses into the carboxysome so slowly that RuBisCO consumes CO_2 as quickly as it is produced. For incremental decreases in k_c in this range, it takes a higher j_c to produce the needed concentration of HCO_3^- in the cytosol to drive diffusion of HCO_3^- into the carboxysome at the same rate.

We will discuss how restricting carboxysome permeability can have a positive effect on CO_2 concentration momentarily. First we want to find second solution in Fig. 1.3.2, where carbonic anyhdrase is saturated, so that we can define where the transition to this regime takes place.

1.3.2 Carbonic Anhydrase is saturated

The solution when carbonic anhydrase is saturated, as it is above the critical j_c in Fig 1.3.2, can be found by assuming the forward reaction is saturated and solving the resulting equation. The forward reaction, HCO_3^- to CO_2, is saturated when $H >> K_{ba}$. As a result, the production of CO_2 is now constant and cannot increase with more HCO_3^- transport. Using these two inequalities and keeping only the large terms as an approximation, $\nabla^2 H = \frac{Vba}{D}$ and $\nabla^2 C = -\frac{Vba}{D}$, implying

$$C_{carboxysome} = -\frac{V_{ba}}{6D}r^2 + A_1 \tag{1.21}$$

$$H_{carboxysome} = \frac{V_{ba}}{6D}r^2 + B_1 \tag{1.22}$$

Here we have imposed that the solution cannot diverge at $r = 0$. The constants A_1 and B_1 are set by coupling these solutions with the solution in the cytosol, equations (1.13) and (1.14), using boundary conditions (1.9) and (1.10). Despite the solution now being dependent on the radial position, it ends up being mostly constant across the carboxysome.

The black line in Fig. 1.3.1 indicates the HCO_3^- transport, j_c, and carboxysome permeability, k_c which result in carbonic anyhdrase becomes saturated. The critical j_c and k_c values are set by the transition between carbonic anyhdrase being unsaturated to saturated, or where equation (1.17) is equal to equation (1.21). Unlike the red and blue lines, which indicate a particular CO_2 concentration has been reached, the black line indicates when the transition between two solutions happens, but tells us nothing about the concentration at that transition. To the right of the line, CO_2 concentration does not depend on j_c, and the concentration will be set by equation (1.21).

The black line in Fig. 1.3.1 shows that for high values of k_c, a lower value of j_c is needed to saturate carbonic anhydrase.The linear increase in j_c needed to saturate below $k_c \approx 5e^{-4}\frac{cm}{s}$ is from the same mechanism as described for the red and blue curves; more HCO_3^- is needed in the cytosol to produce the same rate of diffusion into the carboxysome.

We have defined the region where the carbon concentrating mechanism is most effective, between RuBisCO saturation, the red line in Fig 1.3.1, and carbonic anhydrase saturation, the black line in Fig 1.3.1. Within this region there are many values of j_c and k_c which will result in the same CO_2 concentration. We have defined one of these constant concentration lines, the blue curve in Fig 1.3.1, where there is 1% oxygenation error rate. Generally, moving to the right and increasing j_c within the region between the red and black lines will result in higher CO_2 concentration in the carboxysome. However, the same change in j_c will have varying magnitude of effect depending on what the carboxysome permeability. The system can maximize the impact of the same j_c value if the carboxysome permeability is optimal.

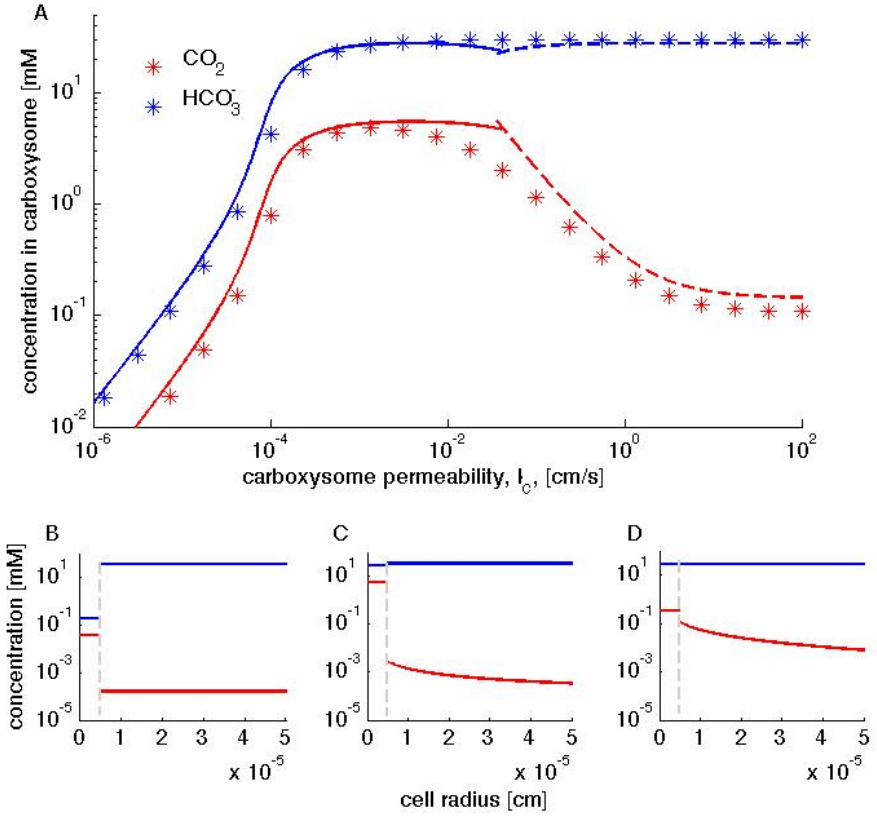

Figure 1.3.3: Concentration of CO_2 in the carboxysome with varying carboxysome permeability (A). Numerical solution (astricks), analytic solution with carbonic anhydrase equilibrating CO_2 and HCO_3^- (solid lines), and analytic solution with carbonic anhydrase is saturated (dashed lines) are shown. On all plots CO_2 is red and HCO_3^- is blue. Concentration in the cell along the radius, r, with carboxysome permeability $k_c = 1e^{-5}\frac{cm}{s}$ (B), $k_c = 1e^{-3}\frac{cm}{s}$ (C), $k_c = 1\frac{cm}{s}$ (D). Grey dotted lines in (B), (C), (D) indicate location of the carboxysome shell boundary. The transition from low CO_2 at high permeability (D) to maximum CO_2 concentration at optimal permeability(C) occurs at $k_c^* = \frac{D}{R_C} = 2\frac{cm}{s}$. Restriction of diffusion of HCO_3^- into the carboxysome begins to become a problem at $k_c << k_c^*$ (B). For all subplots $a = 0\frac{cm}{s}$ and $j_c = 0.7\frac{cm}{s}$.

1.4 Benefit of carboxysome permeability

The carboxysome permeability has an effect on the CO_2 concentration in the carboxysome, even without any special selectivity. There is an optimal

carboxysome permeability, as shown in Fig. 1.3.3. The CO_2 concentration in the carboxysome is low at high permeability (Fig. 1.3.3B), maximum for some optimal value (Fig. 1.3.3C), and low again at low permeability (Fig. 1.3.3D). We examine varying values of carboxysome permeability, k_c, with all other parameters, including j_c, held fixed.

At high permeability, the CO_2 produced in the carboxysome rapidly leaks out of the carboxysome, producing a relatively high CO_2 concentration in the cytosol. Since the cell membrane is very permeable to CO_2, the relatively high CO_2 concentration in the cytosol results in high rate of CO_2 leakage. When the time to diffuse out of the carboxysome, or through the shell, $\tau_{k_c} = \frac{R_c}{k_c}$ is larger than the time to diffuse across the carboxysome, $\tau_{R_c} = \frac{R_c^2}{D}$ then the carboxysome begins to trap CO_2. The transition happens when $k_c < \frac{D}{R_C} = 2\frac{cm}{s}$ in Fig 1.3.3A.

HCO_3^- diffusion across the carboxysome becomes restricted when diffusion of HCO_3^- into the carboxysome cannot keep up with consumption from RuBisCO. We can find this transition analytically as the place where the concentration of CO_2 consumed by RuBisCO is the same order of magnitude concentration of CO_2 in the carboxysome without RuBisCO, which happens at $k_c \approx 1e^{-4}$ in Fig. 1.3.3. It turns out that the concentration of CO_2 consumed by RuBisCO is inversely proportional to carboxysome permeability, $C_{Rub} \approx \frac{R_c V_{max}}{3k_c}$ for the carboxysome permeability near the optimum. So as the permeability decreases this term grows larger. We can see the effects of restriction by comparing the HCO_3^- concentration profile across the cell (blue line) in Fig 1.3.3B, where there is a discrete jump at the carboxysome shell, to that in Fig 1.3.3(C and D), where the HCO_3^- concentration is nearly constant across the carboxysome shell.

In principle we can find the optimal carboxysome permeability value by maximizing equation (1.17) and solving for k_c. However, since the resulting equation would be very bulky it might be more useful to use the intuition that the optimal will happen when $k_c < k_m^H \frac{R_b^2}{R_c^2}$ or $k_c^* \approx 1e^{-3}$ in Fig. 1.3.3(A and C). This expression says velocity of carbon in an out of the carboxysome, k_c, multiplied by the time to diffuse across the carboxysome, τ_{R_c} is less than the velocity of HCO_3^- across the cell membrane, multiplied the time to diffuse across the cell, τ_{R_b}.

Another way of putting it is that the carbon pool in the carboxysome and cytosol are effectively separated, as diffusing in and out of the carboxysome has become the limiting step.

When k_c is at the optimal value, the CO_2 produced in the carboxysome is trapped, as shown in the difference in CO_2 concentration in the carboxysome between Fig. 1.3.3C and Fig. 1.3.3D. Trapping CO_2 in the carboxysome reduces the CO_2 concentration at the cell membrane so the cell membrane is mostly bombarded by HCO_3^-. Therefore the leakage rate of carbon out of the cell is set by the very low k_m^H instead of k_m^C.

1.5 Benefit of α activity: facilitated uptake or scavenging

In Fig. 1.5.1 we investigate the effect of CO_2 to HCO_3^- conversion at the cell membrane. Increasing conversion, $\alpha > 0$, can facilitate uptake of CO_2 from outside the cell and scavenge CO_2 escaped from the carboxysome. Facilitated uptake results in saturating both carbonic anhydrase and RuBisCO at a lower level of HCO_3^- transport, seen as a shift in the black and red curves to the left in Fig.1.5.1. Scavenging broadens the range of carboxysome permeability which will effectively separate the carbon pools in the carboxysome and outside, creating a broader range of 'optimal' carboxysome permeability.

The relative effects of these two mechanisms depends on the external CO_2 and HCO_3^- concentrations. In saltwater environments HCO_3^- is the predominant inorganic carbon source and thus far we have assumed low inorganic carbon concentrations of $[CO_2] = 0.1\mu M$ and $[HCO_3^-] = 14.9\mu M$. The effect of facilitiated uptake under these assumptions is very small. In freshwater there can be a much larger proportion of CO_2. Fig. 1.5.2 shows the absolute contribution of HCO_3^- transport, facilitated CO_2 uptake, and CO_2 scavenging for varying proportions of external CO_2. Even though we assume the same velocity of facilitated uptake and HCO_3^- transport, facilitated uptake contributes less because it is limited by CO_2 diffusion across the membrane.

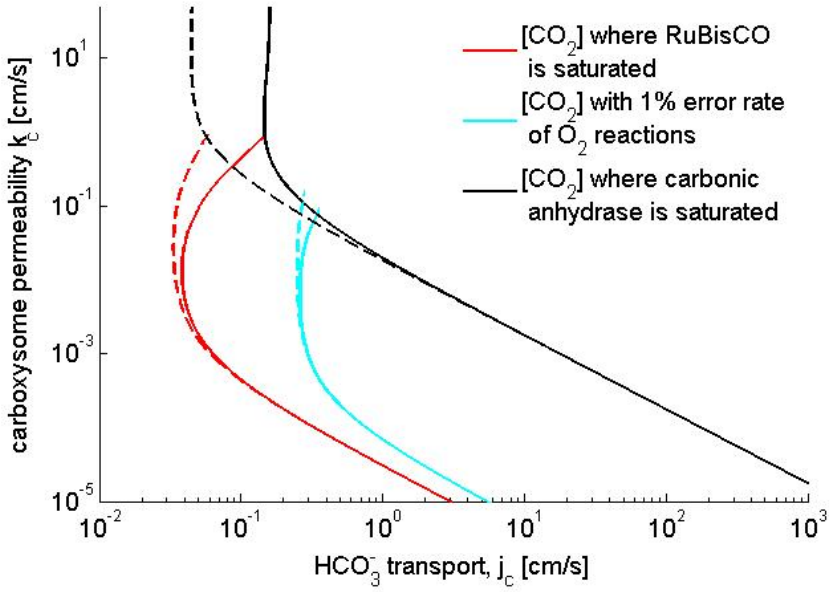

Figure 1.5.1: Phase space for $\mathrm{HCO_3^-}$ transport and carboxysome permeability. The same critical values are plotted as in Fig 1.3.1 when $a = 0\frac{cm}{s}$ (solid lines). The dotted lines show the shift when $a = 1\frac{cm}{s}$, and there is non-negligible $\mathrm{CO_2}$ scavenging and facilitated uptake. All other parameters, such as reaction rates are held fixed and the value can be found in tables A.0.1 and A.0.2.

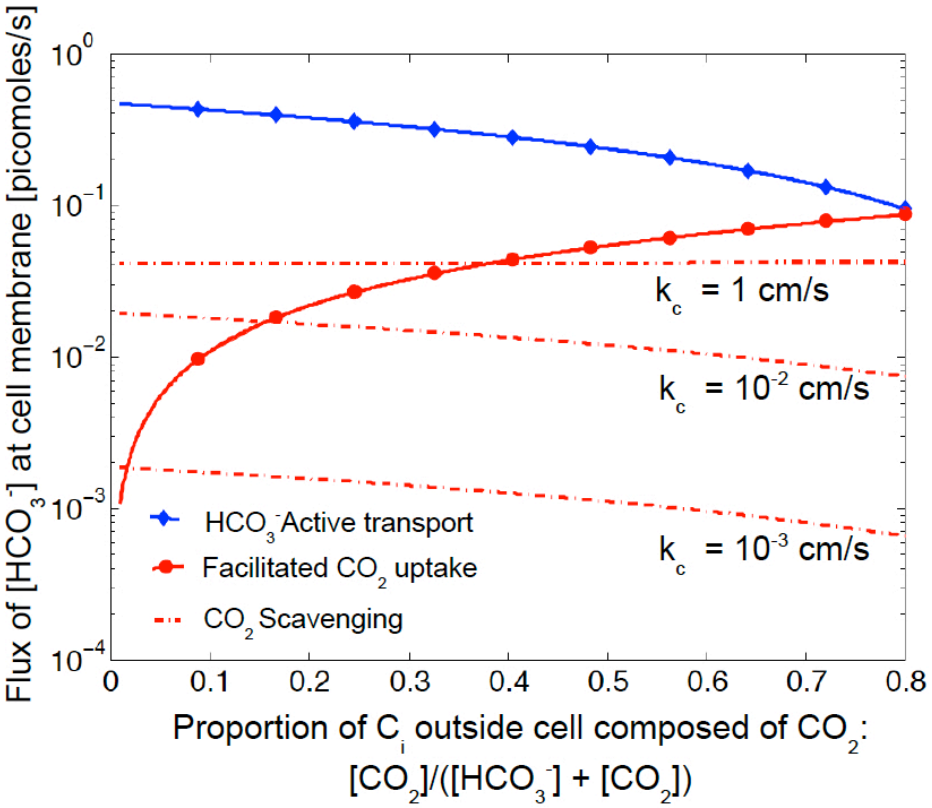

Figure 1.5.2: Size of the HCO_3^- flux in one cell from varying sources, as the proportion of CO_2 to HCO_3^- outside the cell changes changes. We show results for three values of k_c, and only the scavenging is effected. Total external inorganic carbon is $15\mu M$, $j_c = 1\frac{cm}{s}$ and $\frac{a}{K_a} = 1\frac{cm}{s}$. When the carboxysome permeability is larger than optimal, $k_c = 1\frac{cm}{s}$, scavenging can contribute more than facilitated uptake at low external CO_2 concentrations. However, when the carboxysome permeability is optimal, $k_c = 1e^{-3}\frac{cm}{s}$, scavenging is negligibly small. Unless there is very little HCO_3^- in the environment, HCO_3^- transport seems to be more efficient than CO_2 facilitated uptake.

Scavenging only contributes significantly when the carboxysome permeability is higher than optimal, Fig. 1.5.2A. Scavenging decreases the concentration of CO_2 in the cytosol, so a more permeable carboxysome can still result in a low leakage rate out of the cell. The optimal carboxysome permeability threshold is then modified by the proportional rates of CO_2 conversion to leakage, $k_c < \frac{(k_m^C + \frac{a}{K_a})}{k_m^C} k_m^H \frac{R_b^2}{R_c^2}$. This threshold is highly dependent on the cell membrane permeability to CO_2 and HCO_3^-. If the cell membrane permeability were lower, scavenging would have a much larger effect. When the carboxysome permeability is optimal, there is very little CO_2 leaking out of the carboxysome into the cytosol, so there is very little CO_2 to scavenge, Fig. 1.5.2B.

1.6 Discussion

1.6.1 Cellular organization

We compare the effect of localizing carbonic anhydrase and RuBisCO to some small region as opposed to encapsulating them in a compartment, Fig. 1.6.1. There is almost an order of magnitude increase in the concentration of CO_2 when carbonic anhydrase and RuBisCO go from being distributed throughout the cell to concentrated in a small region in the center of the cell. Localizing the carbonic anhydrase to a small volume concentrates it, increasing the maximum reaction rate per volume V_{ca} and V_{ba}. The equation for CO_2 concentration in the carboxysome with saturated carbonic anhydrase, equation (1.21), is proportional to V_{ba}. Therefore, increasing V_{ba} will increase the HCO_3^- transport, j_c, which saturates carbonic anhydrase allowing for a higher possible CO_2 concentration. A small increase can be gained from encapsulating the enzymes in a permeable carboxysome shell and another order of magnitude is gained at the optimal permeability, as previously discussed.

Another advantage of localizing the enzymes in a small region at the center of the cell is separating carbonic anhydrase from the a conversion mechanism, preventing a vicious cycle. The vicious cycle is most detrimental when the

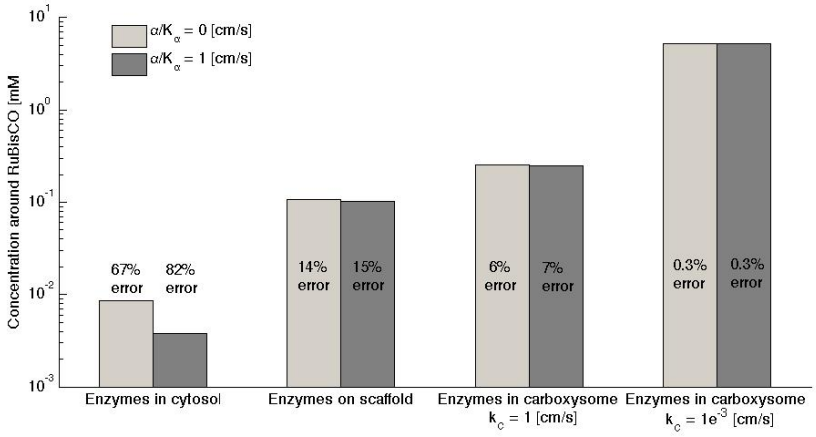

Figure 1.6.1: Concentration of CO_2 achieved through various cellular organizations of enzymes, where we have selected the HCO_3^- transport level such that the HCO_3^- concentration in the cytosol is $30mM$. The oxygenation error rates, as a percent of total RuBisCO reactions are indicated on the concentration bars. The cellular organizations investigated are RuBisCO and carbonic anhydrase distributed throughout the entire cytosol, co-localizing RuBisCO and carbonic anhydrase on a scaffold at the center of the cell without a carboxysome shell, RuBisCO and carbonic anhydrase encapsulated in a carboxysome with high permeability at the center of the cell, and RuBisCO and carbonic anhydrase encapsulated in a carboxysome with optimal permeability at the center of the cell. We show each of these configurations with $\alpha = 0\frac{cm}{s}$ (light grey) and $\alpha = 1\frac{cm}{s}$ (dark grey).

enzymes are distributed through out the cytosol, when $a = 1$, as shown in dark grey on Fig 1.6.1. Concentrating the enzymes away from the cell and thylakoid membranes, where conversion happens, removes this effect. At optimal carboxysome permeability, the carbon pools are effectively separated and conversion can act only as facilitated uptake.

When the carboxysome permeability is optimal, and effectively separates the carbon pools in the carboxysome and cytosol, there cannot be a significant gradient in HCO_3^- across the cell. If there is no significant gradient in HCO_3^-, then the position of the carboxysome in cell does not matter. Additionally, there is no optimal positioning of other carboxysomes to avoid competition for HCO_3^-.

1.6.2 Where are the physiological carbon concentrations?

While carbon uptake measurements vary between systems and often rely on a model to interpret, inorganic carbon pool measurements are relatively simple to interpret and consistent across experiments. At low external carbon conditions, internal inorganic carbon pools are regularly measured to be around $C_i = 30mM$ [24, 36, 39, 55, 64]. This carbon pool has been found to be predominantly HCO_3^-, a result which we recapitulate. As shown in Fig. 1.3.3(A, B, C), CO_2 concentration is a few percent of total inorganic carbon in the cytosol. Therefore, HCO_3^- concentration in the cytosol is representative of the size of the carbon pool. The values of HCO_3^- transport, j_c, and carboxysome permeability, k_c, where our model results in $HCO_3^- = 30mM$ in the cytosol are indicated by the dashed grey line in Fig. 1.6.2. The HCO_3^- concentration is basically independent of the carboxysome permeability in this parameter regime, and $j_c \approx 0.7\frac{cm}{s}$ results in a carbon pool of $\approx 30mM$. In this regime, when external inorganic carbon is primarily HCO_3^-, facilitated uptake and scavenging play a negligible role and don't greatly effect the CO_2 concentration in the carboxysome.

For $j_c = 0.7\frac{cm}{s}$, there is enormous variation in the CO_2 concentration in the carboxysome with varying carboxysome permeability as shown in Fig 1.3.3. At

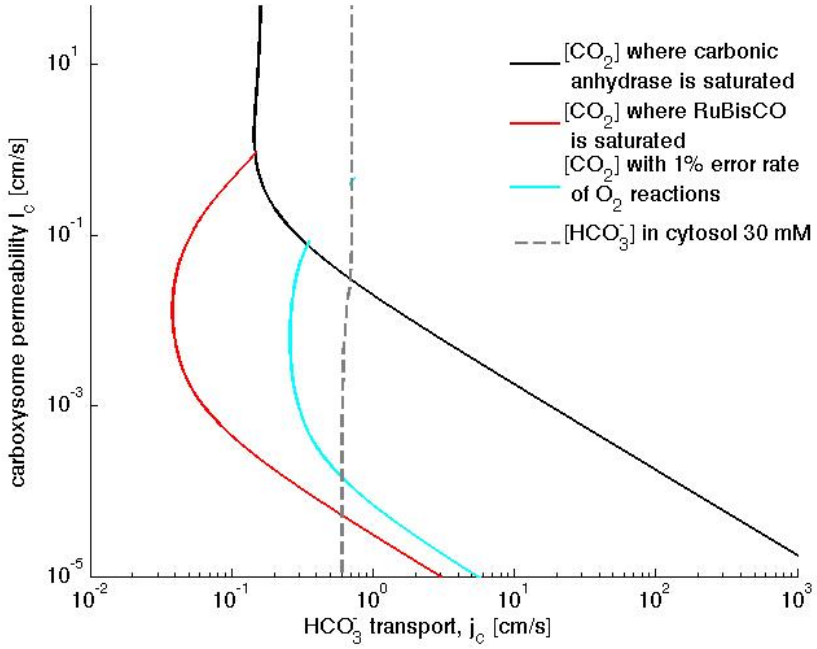

Figure 1.6.2: Phase space for HCO_3^- transport and carboxysome permeability. The same critical values are plotted as in Fig 1.3.1 when $a = 0\frac{cm}{s}$ (solid lines). The grey dotted line shows the k_c and j_c values, where the HCO_3^- concentration in the cytosol is $30mM$. The HCO_3^- concentration in the cytosol does not vary appreciably with k_c and reaches $30mM$ at $j_c \approx 0.7\frac{cm}{s}$. All other parameters, such as reaction rates are held fixed and the value can be found in tables A.0.1 and A.0.2.

the optimal carboxysome permeability, the CO_2 concentration in the carboxysome is about 5*mM* shown in Fig. 1.3.3A and C, compared to 0.1*mM* or lower in the non-optimal carboxysome permeabilities, shown in Fig. 1.3.3A, B, and D. A CO_2 concentration of 5*mM* results in 0.33% oxygenation error rate or 66 in every 10,000 reactions are oxygenations.

2

Melting and solute dynamics of hyperdoping with femtosecond-laser

2.1 Introduction

Hyper-doping with femto-second lasers offers a versatile method for creating a variety of new materials including semi-conductor materials doped at beyond the equilibrium solubility limit [6, 60, 61, 65, 68]. Silicon hyper-doped with sulfur has been shown to absorb more highly in the infra-red region, already has applications such as night-vision sensors and is being explored for other uses such as photovoltaics [28, 30, 35]. For current and future applications, being able to finely tune the dopant profile in the material will allow more efficient and effective devices. Experimental evidence shows that the dose and dopant distribution in the material can be altered by changing laser fluence, pulse

number, and pressure of gaseous dopant in the reaction chamber [15, 49, 62]. One of the first steps to gaining better control over the doping profile is developing a model which correctly represents the physics in the system. Modeling the melting dynamics and sulfur diffusion into the material allows a greater understanding of the experimental results. A thermal model produces melt dynamics and solute profiles consistent with experimental data. We identify two distinct mechanisms which account for the characteristic dopant profiles in experiments. A change in laser absorption such that melt depth increases or a change in the mechanism of dopant integration from an 'instant' surface dose to a surface flux can both account for changes in dopant profile with subsequent laser pulses.

2.1.1 Experimental Motivation

To dope Si with S, a Si wafer is placed in a chamber filled with SF_6. The material is then irradiated with a femto-second laser pulse. Initially the 800 nm laser pulse lasting about 80 femto-seconds, excites electrons in the material. If enough of the electrons are excited (10-15% of valence electrons) the lattice destabalizes and transitions to a liquid in a process called non-thermal melting [48, 52]. At lower laser pulse energies the lattice remains stable, and the electrons relax back down after about 1ps, transferring their energy to the lattice, in a process called thermalization [56]. In this case, if the energy transfered is above the melting threshold, the heat diffuses through the silicon and melting begins from the surface [63]. As the material melts, energy is used in the melting and heat diffuses into the silicon substrate. Eventually there is not enough localized heat energy to melt the material further, the melting stops and then the material begins to resolidify. The melting and re-solidification process takes place on the time scale of a few nano-seconds. At a laser fluence of $2.5 \frac{kJ}{m^2}$, the material resolidifies as crystalline [49].

During melting, sulfur enters into the material and is incorporated into the silicon in non-equilibrium concentrations [3, 26, 42, 61] . Experiments done by

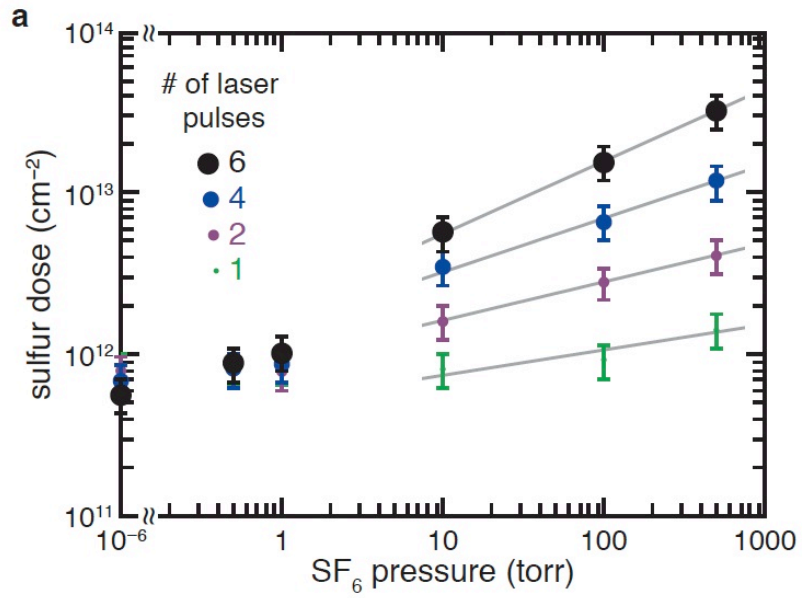

Figure 2.1.1: The total integrated sulfur dose incorporated into the material at varying pressures for different shot numbers. The laser fluence is at 2.5$\frac{kJ}{m^2}$ for each shot. Below 1 torr the dose does not vary appreciably with pressure. At and above 10 torr there is dramatic increase in dose with pressure and shot number. Used with permission from [49].

Sher et al. show that there is a critical pressure below which the incorporation of the dopant into the material is independent of the pressure (Fig. 2.1.1)[49]. Before laser irradiation a layer of SF_6 adsorbs onto the surface of the Si wafer. At low pressures only this adsorbed layer worth of SF_6 is incorporated into the material. Above the critical pressure, the dopant dose, d_S, is dependent on the pulse number, n and pressure, P. Ser et al. found $d_S \propto P^n$, with $n < 1$ [49]. The increase in dose with shot number above a critical pressure threshold comes from a new surface layer forming between each shot above the critical pressure. If the increase in dose with pressure were due to an increased number of SF_6 impinging on the surface, the pressure dependence would be $n = 1$, since bombardment would be linear with pressure. The increase in dose with pressure is most likely due to an increase in the size of the adsorbed layer with increasing pressure [7, 49–51]. The relationship between the pressure in the chamber and

size of adsorbed layer is still under investigation, and not easily described [49]. The exact mechanism for incorporation of the adsorbed layer into the material is unknown and one of the aspects we investigate.

The profile of the dopant in Si has a particular shape. The length scale associated with the penetration depth of S into the material increases with shot number, which we can see at both $P = 0.5$ torr (Fig. 2.1.2A) and $P = 500$ torr (Fig. 2.1.2B). The $P = 0.5$ *torr* data has the same characteristic shapes as data at other pressures below the critical pressure threshold. The length scale is set by dopant diffusion and the melt duration. The material melts much deeper than the dopant diffuses and then solidifies "freezing" the dopant profile at the depth it has reached through diffusion. It is unclear whether the melting dynamics are identical for each laser pulse. Alternatively, the melt depth could increase during later shots because of changes to the material. For example, the introduction of dopant or damage to the material, amorphization, could increased laser absorption. Amorphization is not observed in optical characterization of the material [49]. There is also some uncertainty in the dopant profiles due to the secondary ion mass spectrometry (SIMS) measurement method, which pushes dopant further down into the material during the measurement process.

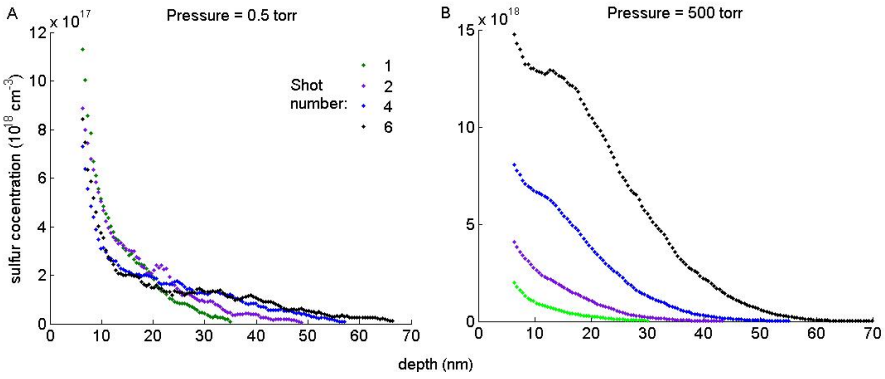

Figure 2.1.2: Secondary ion mass spectrometry (SIMS) measurement of the concentration of sulfur in silicon with depth. Adapted from [49].

The $P = 500$ *torr* data is representative of the profile shapes above the

pressure threshold. Shots 1 and 2 look smooth and approximately exponential. Shots 4 and 6 have a quick decline at followed by a plateau a between 10 and 20 *nm* and then smooth exponential decline. As previously mentioned the sulfur depth increases with increasing shots, and we do not know if the melting dynamics change significantly with increasing shots. We investigate whether this change from exponential to plateau comes from changes in the melting dynamics or from the variation in the sulfur incorperation mechanism. We propose mechanisms for sulfur incorporation, in the form of initial and boundary conditions. The goal of the model is to determine whether these mechanisms can be further differentiated from the data, and determine which parameters control the final dopant profile.

2.2 Physical model of femto-second laser irradiation and S diffusion in Si

2.2.1 Laser Absorption

Since the laser pulse and energy thermalization happen on such a fast time scale, the actual deposition of the energy into the material can be considered as an initial condition to the melting dynamics.

The attenuation of the light intensity, I, due to linear and non-linear free carrier absorption as a function of the depth of the material, x, is described by:

$$I_x = -\alpha I - \beta I^2 \tag{2.1}$$

Where α and β are the linear and nonlinear absorption coefficients respectively. This equation assumes any reflected light has already been accounted for [27]. The initial temperature profile in the material, after the energy thermalizes in the lattice, is related to this equation by:

$$T(x,0) = T_{ambient} + \frac{t_{pulse}}{C_p} I_x \tag{2.2}$$

Here t_{pulse} is the effective duration of the laser and C_p is the volumetric heat capacity of Si. Finding the solution to equation (2.1), assuming $I(x=0) = I_0$, we find

$$T(x,0) = T_{ambient} + \frac{t_{pulse}\alpha^2(\alpha + I_0\beta)I_0 e^{\alpha x}}{C_p(I_0\beta - (\alpha + I_0\beta)e^{\alpha x})^2} \tag{2.3}$$

I_0 is related to the laser fluence, P_{flux}, by $I_0 = \frac{P_{flux}}{t_{pulse}}$ where P_{flux} has units $\frac{kJ}{m^2}$.

2.2.2 Thermal dynamics

We use well established models for nanosecond laser thermal processing [2, 8, 21, 54]. The melting dynamics are determined by thermal diffusion through the material,

$$T_t = (D_T T_x)_x \tag{2.4}$$

energy conservation at the interface,

$$L_v h_t = \kappa_T T_x|_S - \kappa_T T_x|_L \tag{2.5}$$

and the interface response function,

$$h_t = \mu(T(h,t) - T_{melt}). \tag{2.6}$$

Here h is the position of the liquid-solid interface, h_t is the interface velocity, and (2.5), (2.6) describe the movement of the interface and its influence on the thermal gradients. Equation (2.5) accounts for the flux of energy in the liquid and the solid, as indicated by the subscripts L and S, required for melting or solidifying. The latent heat, L_v, is constant. In equation (2.6), μ is the experimentally determined kinetic undercooling coefficient, which encapsulates information about how quickly the interface can move [22]. The thermal conductivity, κ_T, volumetric heat capacity and thermal diffusivity, D_T, are related as follows: $\kappa_T = D_T C_\rho$. They are functions of the temperature of the material, whether it is in the liquid, crystalline or amorphous state, and very weakly with

the solute concentration.

The boundary condition at the surface is formally a radiative condition, but the radiation is very small and so the boundary condition can be approximated as a no-flux boundary condition.

$$T_x|_{x=0} = 0. \tag{2.7}$$

Very far from the surface the temperature should go to the ambient temperature. The silicon wafers used are much deeper (400 μm)than the melting, so this is effectively a semi-infinite boundary problem.

$$T|_{x\to\infty} = T_{ambient} \tag{2.8}$$

2.2.3 Solute dynamics

The dynamics of sulfur diffusion and incorporation into the solid silicon is described by diffusion,

$$C_t = (D_d C_x)_x, \tag{2.9}$$

where the diffusivity of sulfur in silicon, D_d is a function of temperature and zero in the solid. A mass conservation equation at the interface

$$(C^L - C^S)\dot{h} = [-D_d C_x]_{L-S} = -D_d C_x|_L \tag{2.10}$$

sets the flux. Here C^L is the concentration on the liquid side and C^S on the solid. There is no diffusion in the solid (2.10), so only the liquid term remains. An interface condition

$$\frac{C^S}{C^L} = \frac{k_e + \frac{\dot{h}}{v_D}}{1 + \frac{\dot{h}}{v_D}}. \tag{2.11}$$

is also needed to couple the concentration in the liquid and solid [2]. Here, k_e is the equilibrium partition coefficient, and v_D is a kinetic parameter called diffusive velocity. For low solidification velocities, $h_t << v_D$, the sulfur will partition into

the solid and liquid silicon as if it were at equilibrium. When the solidification velocity is larger than the rate at which sulfur can escape from the interface via diffusion, $h_t > v_D$, a larger than equilibrium proportion of sulfur will become trapped.

The experimental data suggests that the dose of S getting in with each shot comes from an adsorbed surface layer, however it is unknown how this dose gets into the material during melting. We propose two methods of incorporation, an "instant dose", which can be represented in a initial condition, or slow diffusion into the material, which can be represented as a flux at the surface.

If the sulfur comes in as an "instant dose" it is an initial condition is a sharp square function.

$$C_0 = \begin{cases} C_{surface}(P,i) & \text{for} \quad x < \delta x \\ 0 & \text{for} \quad x > \delta x \end{cases} \tag{2.12}$$

Here $C_{surface}$ is the surface layer from absorption which is a function of pressure, P, and shot number, i. The concentration begins in a small region δx. If we are simulating multiple shots then we save concentrations from previous shots and write the intial condition as,

$$C(x,0) = C_i(x) + C_0, \tag{2.13}$$

where C_i is the concentration left after the ith shot. We write a flux boundary condition, where the flux depends on the pressure and shot number,

$$C_x|_{x=0} = J_c(P,s) \tag{2.14}$$

If we are assuming that the whole dose comes from an "instant dose" in the initial condition, then we set $J_c = 0$. If we assume the whole dose comes from surface flux, we set $C_{surface} = 0$.

To close the system of equations we also need a boundary condition as

$x \to \infty$,

$$C|_{x\to\infty} = 0. \tag{2.15}$$

2.2.4 Parameter ranges

Many of the parameters in this model are well known and do not vary. Others such as laser fluence, shot number, and chamber pressure are under experimental control. The only parameter which is unknown is the nonlinear absorption coefficient, but using nonlinear coefficients measured for other laser wavelengths, we can assume a range. We also do not know the exact conversion between the experimental laser fluence and the laser fluence in our model, since some of the energy (about 40%) will be reflected. All parameters are summarized in table 2.2.1.

Table 2.2.1: Simulation parameters.

Parameter	symbol	value	units	reference
laser fluence	P_{flux}	1.05 to 2.77	$\frac{kJ}{m^2}$	[49]
linear absorption	α	$2.25e^5$	$\frac{1}{m}$	[27]
nonlinear absorption	β	$9e^7$ to$8e^9$	$\frac{mfs}{kJ}$	[27]
laser pulse duration	t_{pulse}	80	fs	[49]
volumetric heat capacity	C_ρ	$2414e^3$	$\frac{kJ}{m^3K}$	[21]
thermal conductivity crystaline at melting temp	κ_T^S	$22e^3$	$\frac{kJ}{msK}$	[21]
thermal conductivity liquid	κ_T^L	$140e^3$	$\frac{kJ}{msK}$	[21]
thermal diffusivity	D_T	$\frac{\kappa_T}{C_\rho}$	$\frac{m^2}{s}$	[21]
latent heat	L_v	4206	$\frac{J}{cm^3}$	[21]
kinetic undercooling	μ	0.0667	$\frac{m}{sK}$	[22]
diffusivity of sulfur in silicon	D_d	$2.7e^{-4}$	$\frac{cm^2}{s}$	[54]
equilibrium partition coefficient	k_e	$1e^{-4}$	$\frac{m}{sK}$	[22]
diffusive velocity	v_D	1	$\frac{m}{s}$	[54]
pressure	P	$1e^{-6}$ to 500	torr	[49]
shot number	s	1 to 6		[49]

We find the melting dynamics over a range of parameters by numerically solving the equations. We then use experimental constraints on the melting dynamics to constrain the parameters further. From the dopant profiles, we know the melt depth must be between, $30 < x_m < 80\ nm$ where there is some error from the SIMS measurement $(\pm 5nm)$. If the melting dynamics do not vary with shot number, then the melt depth would have to be $x_m > 60\ nm$. If the melting dynamics vary with shot then the melt depth would have to increase with shot number across the range. The resolidification velocity must be, $v_r < 15\ \frac{m}{s}$, in order to produce crystaline material as opposed to amorphous [53, 58].

2.3 Numerical Methods

For the numerical treatment of the model we reduce the number of parameters by dimensional analysis and write the equations in non-dimensional form. The non-dimensional, free-interface Stefan's problem is then transformed into a coupled advection-diffusion problem on a fixed domain. This allows numerical integration without necessitating re-meshing at every time step or other sophisticated techniques, but introduces a singularity as the position of the solid-liquid interface approaches zero (the surface). We find asymptotic solutions for early times, where the singularity occurs and use them as an initial condition in the numerical solution of the full equation system. When the material solidifies, the equations once again diverge and we enforce mass conservation of the solute near the surface. In this section we describe the mapping and the aymptotic matching, the methods for numerical integration, the asymptotic solution for early times, treatment of the infinite boundary condition, and enforcement of mass conservation at the end of the simulation.

2.3.1 Non-dimensional form of the equations

We introduce characteristic scales for length, L, temperature, Θ, concentration, C_0, time, τ, and thermal diffusivity, κ_τ^* such that,

$$x = L\hat{x} \tag{2.16}$$

$$T = \Theta\hat{T} + T_{ambient} \tag{2.17}$$

$$C = C_0\hat{C} \tag{2.18}$$

$$t = \tau\hat{t} \tag{2.19}$$

$$\kappa_T = \kappa_T^*\kappa_T \tag{2.20}$$

All diffusion constants are normalized by $\overline{D} = \frac{L^2}{\tau}$. We set $\Theta = T_{melt} - T_{ambiant}$ so that $\hat{T}_{melt} = 1$ and $\hat{T}_{ambient} = 0$. The non dimensional evolution equations for $\hat{T}$, $\hat{C}$, and $\hat{h}$ are

$$\hat{T}_{\hat{t}} = \left(\hat{D_T}\hat{T}_{\hat{x}}\right)_{\hat{x}} \tag{2.21}$$

$$\hat{C}_{\hat{t}} = \left(\hat{D_d}\hat{C}_{\hat{x}}\right)_{\hat{x}} \tag{2.22}$$

$$\hat{h}_{\hat{t}} = \mathcal{A}\left[-\hat{\kappa_T}\hat{T}_{\hat{x}}\right] \tag{2.23}$$

$$\left[\hat{C}\right]\hat{h}_{\hat{t}} = -\hat{D_d}\hat{C}_{\hat{x}}|_{\hat{x}=\hat{h}^-} \tag{2.24}$$

with the rescaled thermal diffusivity,

$$\mathcal{A} = \frac{\Theta\tau\kappa_T^*}{L^2L_V} \tag{2.25}$$

as the remaining non-dimensional parameter. These are supplemented by the non-dimensional boundary conditions for temperature $\hat{T} \to 0$ for $\hat{x} \to \infty$ and at the surface $(\hat{x} = 0)$, where $\hat{T}_{\hat{x}} = 0$. The boundary condition for the concentration and interface response function can be made nondimensional using the same scales. We now drop the 'hat' for convenience and all quantities in Section 4 are non-dimensional unless explicitly mentioned.

2.3.2 Mapping equations to a fixed computational domain

Moving boundaries, like the one at $x = h(t)$ are numerically difficult to handle and require sophisticated meshing techniques, where the mesh changes as then interface moves. To avoid these problems and use a straightforward discretatization using finite differences we map the problem to a fixed domain by transforming $x \to \frac{x}{h(t)}$.

The equations are mapped to a fixed domain through the following transformations: $\partial_t \to \partial_t - x' \frac{h_t}{h} \partial_x$ and $\partial_x \to \frac{1}{h} \partial_x$. This transformation maps the equations to a fixed domain where the solid-liquid boundary fixed at $x' = 1$. Omitting the prime, the equations are now written as the following advection-diffusion equations

$$h^2 T_t = (D_T^{(l)} T_x)_x + x h h_t T_x, \quad x \in [0, 1] \tag{2.26}$$

$$h^2 T_t = (D_T^{(s)} T_x)_x + x h h_t T_x, \quad x \in [1, \infty] \tag{2.27}$$

$$h^2 C_t = (D_d^{(l)} C_x)_x + x h h_t C_x, \quad x \in [0, 1] \tag{2.28}$$

$$\tag{2.29}$$

The system is described by three coupled second order PDEs which depend on the intrinsic dynamic parameter h at the interface due to rescaling. We need equations describing the motion of the interface,

$$h h_t = \mathcal{A}[-\kappa_T T_x] \tag{2.30}$$

$$(C|_{x=1} - C^S) h h_t = -D_d C_x|_{x=1^-} \tag{2.31}$$

$$h_t = \hat{\mu}(T - 1) \tag{2.32}$$

These are the conservation of energy an solute at the interface, and the interface response function, where $\hat{\mu}$ is the kinetic undercooling coefficient normalized by $\frac{L}{\tau\Theta}$ We also require the continuity of the temperature field. To close the equations for temperature we need boundary conditions for temperature at

$x \to 0$ and at the surface $x = 0$. These are the same as before, but with non-dimensional temperature and concentration.

To close the concentration equations we need conditions at the interface as well as the surface. For the concentration flux boundary condition, the equation becomes

$$C_x|_{x=0} = hJ_c(P, s). \tag{2.33}$$

The condition at the interface for concentration is

$$C^S = \frac{k_e + \frac{h_t}{v_D}}{1 + \frac{h_t}{v_D}} C|_{x=1}, \quad h_t < 0. \tag{2.34}$$

where v_D has been normalized by $\frac{L}{\tau}$.

We can now numerically solve these equation using a Crank-Nicolson scheme with finite discretization in space.

While this transformation makes numerical meshing to discretize these equations easier, it does introduce a singularity as $h \to 0$. The singularity is a problem at early times since there is no liquid layer at $t = 0$ and again as the material solidifies at the end of the melting dynamics. At the end of the simulation, the interface approaches the surface at a constant velocity, so it is simple to end the simulation at a finite h and then extrapolate the behavior to $h = 0$. The behavior in early times is more complicated and we must develop an asymptotic solution for early time.

2.3.3 Asymptotic solution at early times

We develop an asymptotic solution for the initial melting phase by assuming constant velocity ($h = Ut$) for early times. With these assumptions we can write a Green's function formulation of the dynamics for short times. We then check the validity of these assumptions.

We write the heat diffusion in two domains coupled by the jump condition for

the derivative as equivalent to

$$T_t = (D_T T_x)_x - a h_t \delta(x - h(t)) \tag{2.35}$$

where $a = \frac{L_v}{C_p \Theta}$. We assume D_T constant and set it to the diffusivity at the temperature at the surface at $t = 0$ as determined by equation (2.3).

The melting interface constitutes a moving heat sink whose dynamics are described by the interface response function

$$h_t = \mu(T - T_{melt}). \tag{2.36}$$

We express the temperature solution in terms of Green's functions

$$\begin{aligned} T(x,t) = &\int_0^\infty dx' T(x, t=0) \mathcal{G}(x, x', t', 0) \\ &- a \int_0^t dt' h_t(t') \mathcal{G}(x, h(t'), t, t') \end{aligned} \tag{2.37}$$

with the Green's function

$$G(x, x_0, t, t_0) = \frac{1}{\sqrt{4\pi D_T (t - t_0)}} \left(e^{-\frac{(x-x_0)^2}{4D_T(t-t_0)}} + e^{-\frac{(x+x_0)^2}{4D_T(t-t_0)}} \right). \tag{2.38}$$

Here the spatial integral describes the influence of the initial temperature profile. The time integral describing the melting dynamics contains the source terms, which collapse to a pure time integral due to the spatial delta function in the source.

Assuming $h_t = U$ for some small time $\tilde{t}$ we evaluate the temperature at the interface. Combined with the interface response function
$h_t = \hat{\mu}(T(h, \tilde{t} - 1) = U$ we have an integral equation for the unknown velocity

U.

$$\frac{U}{\mu} + T_{melt} = \int_0^\infty dx' T(x, t=0)\mathcal{G}(U\tilde{t}, x', \tilde{t}', 0) - aU\int_0^{\tilde{t}} dt' \mathcal{G}(U\tilde{t}, h(t'), \tilde{t}, t') \tag{2.39}$$

We can numerically evaluate both integrals. Accurate integration of the time integral requires a transformation of $t \to \tau = \sqrt{\tilde{t} - t}$ to remove divergence at $t = \tilde{t}$. We can then solve for the initial velocity U by solving equation (2.39) using the Newton Method. Once we have found U we can find the whole temperature field by numerically integrating equation (2.37) with $h_t = U$ at time $\tilde{t}$.

We must select a time $\tilde{t}$ such that the assumption of constant interface velocity is valid. We check whether we have chosen a small enough time by simulating the full evolution for $\tilde{t} = t^*$ and $\tilde{t} = 2t^*$ and then making sure the relative error is smaller than 1 %.

2.3.4 Conservation of mass upon solidification

As $h \to 0$ during solidification, we must stop the simulation before h becomes too small, and extrapolate the behavior. We are not concerned with the exact shape of the concentration profile within the first hundredths of a nm at the surface, but we do want maintain conservation of mass for the sulfur. So we stop the simulation at small h and then enforce conservation of mass. For simplicity we extrapolate the concentration field as a gaussian to the surface

$$C = B + Ae^{(-\frac{h^2}{H^2})}. \tag{2.40}$$

We choose length scale H to be sufficiently small compared to h. The coefficients A and B are chosen so that mass is conserved and the concentration at h matches the concentration in the solid at the end of the simulation.

2.3.5 Treatment of infinite boundary condition for temperature

Generally, to deal with the infinite boundary condition numerically we would choose a value L_∞, large enough that changing it has negligible effects on the dynamics. However, an effective boundary condition at finite distance can be derived by asymptotics. Far away from the melting process, the dynamics are simply heat diffusion. We can think of the phase changes happening at the surface as a time dependent sink (during melting) or source (during solidification) at $x = 0$. For $x' >> \sqrt{4D_T t}$ these soruce terms are irrelevant.

Additionally very far from the surface, the laser intensity has only one length scaled determined by the linear absorption. Therefore, the initial temperature is well approximated by exponentials, locally at x',

$$T(x', t^*) = T(x^*, t^*) e^{-\frac{x' - x^*}{\lambda(x^*)}} \tag{2.41}$$

where λ is the appropriate length scale set by the initial temperature profile at x', $\lambda(x') = -\left[\frac{d}{dx} log T(x', t = 0)\right]^{-1}$.

From this we can immediately find the time evolution far from other sinks or sources, where only diffusion is relevant,

$$T(x, t) = T(x, t^*) e^{\frac{D}{\lambda^2(x^*)}(t - t^*)}. \tag{2.42}$$

This equation is valid for $|t - t^*| << \frac{\lambda^2}{D}$ and $|x' - x^*| << \lambda(x^*)$.

2.4 Thermal profile evolution during melting and resolidification

Our simulation allows us to probe the temperature evolution over time in detail not currently available in experiment. Parameters for the simulations are those in table 2.2.1, or as noted in the figures. We can look at the temperature profile in the material during the melting and solidification process, Fig. 2.4.1. The interface moves deeper into the material during melting, slows as the

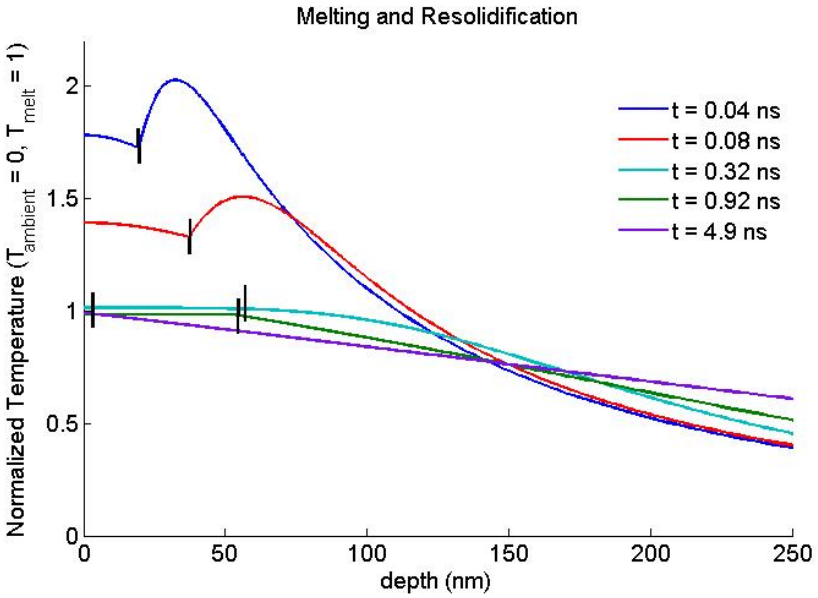

Figure 2.4.1: Snapshots of temperature evolution from simulation with laser fluence, $P_{flux} = 1.4[\frac{kJ}{m^2}]$, and nonlinear absorption coefficient, $\beta = 6e^8[\frac{m\,fs}{kJ}]$. Temperature profiles of melting (t = 0.04, 0.08, 0.32 ns), see Fig. 2.4.2 for more detail, and solidification (t = 0.92 ,4.92 ns), see Fig. 2.4.4 for more detail, where the interface position is marked in black. The transition from melting to solidification happens at t = 0.38 ns, see Fig. 2.4.3 for more detail.

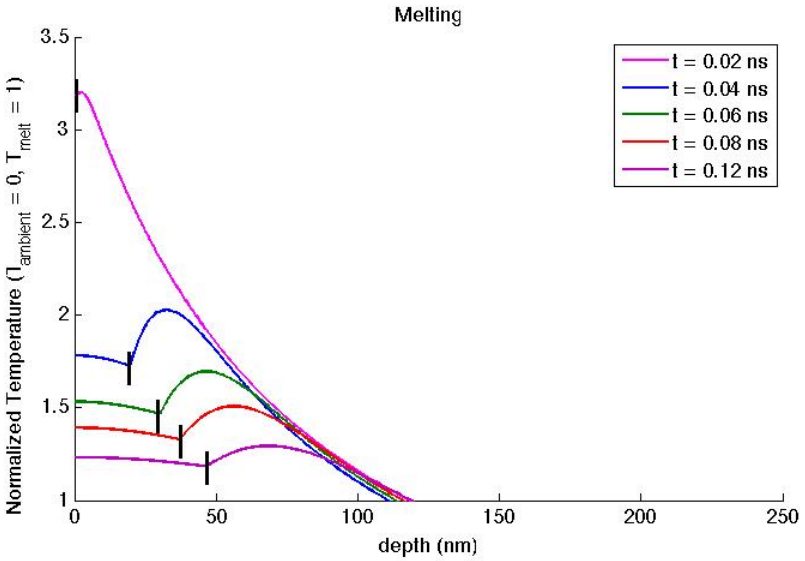

Figure 2.4.2: Snapshots of temperature evolution from simulation with laser fluence, $P_{flux} = 1.4[\frac{kJ}{m^2}]$, and nonlinear absorption coefficient, $\beta = 6e^8[\frac{m\,fs}{kJ}]$. Temperature profiles of melting where the interface position is marked in black. The transition from melting to solidification happens at t = 0.38 ns. The interface is moving away from the surface deeper into the material.

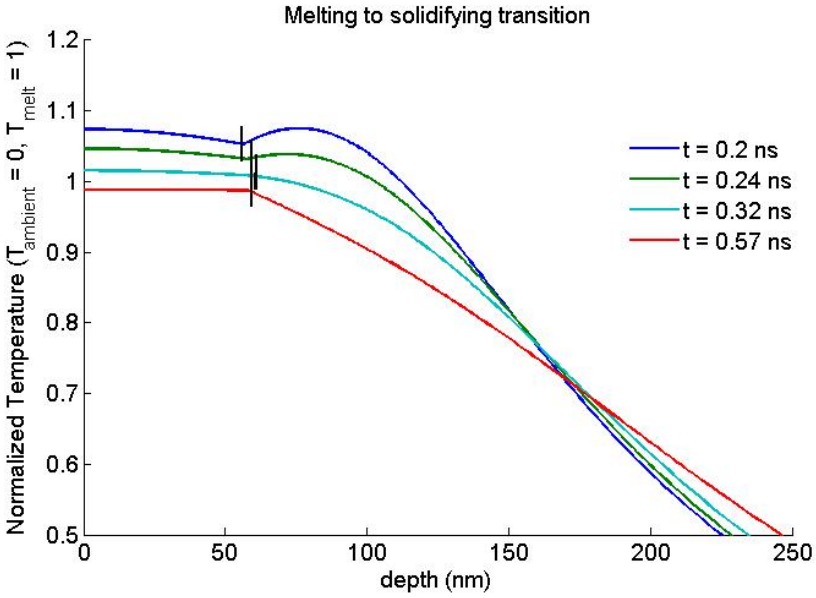

Figure 2.4.3: Snapshots of temperature evolution from simulation with laser fluence, $P_{flux} = 1.4[\frac{kJ}{m^2}]$, and nonlinear absorption coefficient, $\beta = 6e^8[\frac{m\,fs}{kJ}]$. Temperature profiles around the time of transition from melting to solidifying, where the interface position is marked in black. The transition from melting to solidification happens at t = 0.38 ns. The interface moves away from the surface during melting, slows, stops at maximum melt depth, and begins to move back towards the surface during solidification.

temperature profile flattens out, and then moves back toward the surface solidifying. As the material melts, the temperature profile quickly develops a kink where the sink of the moving interface is located, and energy is being used to melt the material, Fig.2.4.2. Close to the transition between melting and solidifying the profile flattens a great deal, slowing the interface, since the speed of the interface is related to the gradients Fig. 2.4.3. As the material solidifies, energy is recovered from the interface, so the temperature in the liquid increases slightly Fig. 2.4.4. The speed of solidification depends on the gradient. The gradient in the liquid is very flat, making the solidification velocity dependent on the gradient in the solid. The magnitude of the gradient in the solid, is set in part

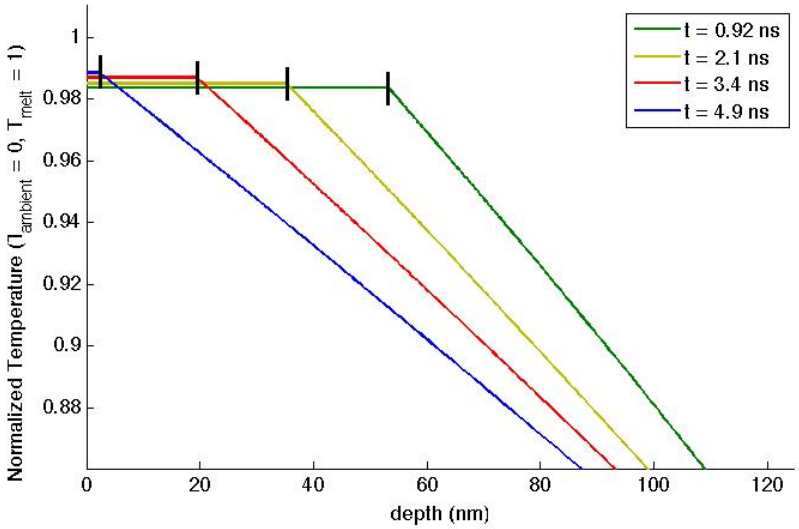

Figure 2.4.4: Snapshots of temperature evolution from simulation with laser fluence, $P_{flux} = 1.4[\frac{kJ}{m^2}]$, and nonlinear absorption coefficient, $\beta = 6e^8[\frac{m\,fs}{kJ}]$. Temperature profiles during solidifying, where the interface position is marked in black. The interface moves towards the surface at later time.

by the initial temperature.

To summarize the melting dynamics we look at the position of the solid-liquid interface over time, Fig. 2.4.5. For the purpose of solute dynamics, the growing and shrinking of the liquid region are most relevent. The interface dynamics are a good summary of the size of the liquid region over time. We find that the interface dynamics are characterized by fast melting period of around $t_1 = 0.5\ ns$ during which the interface rapidly decelerates. The melt depth, x_m, is the maximum interface position. The Silicon solidifies at an almost constant velocity. The time for the entire process, melting and solidification, is the melt duration, t_m. The melting dynamics are very similar to those in nanosecond laser melting [21, 25], except the melting portion of the profile looks different, since there is still energy being added to they system for several nanoseconds and time to melt is longer. We look at the variation of the interface dynamics a range of laser fluence and nonlinear absorption coefficients in Fig. 2.4.6, since these are

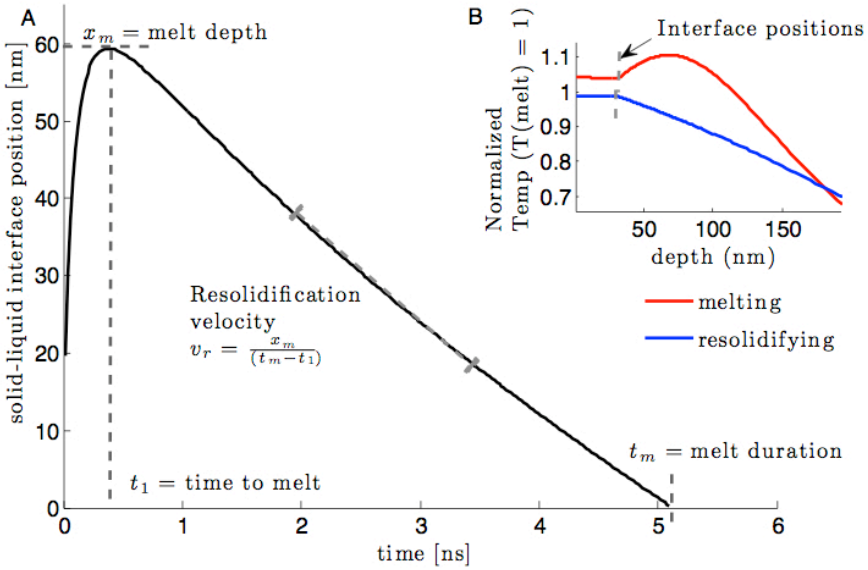

Figure 2.4.5: Summary of melting dynamics found from simulation with laser fluence, $P_{flux} = 1.4[\frac{kJ}{m^2}]$, and nonlinear absorption coefficient, $\beta = 6e^8[\frac{m\,fs}{kJ}]$. The position of the solid liquid interface over time describes the melting dynamics. Temperature profiles of melting (red in inset B) at $t = 0.05[ns]$ and resolidification (blue in inset B) at $t = 2.2[ns]$ where the interface position is at $h = 30[nm]$ and $h = 32[nm]$ respectively. The melt dynamics in (A) are well described by the time to melt, t_1, the melt depth x_m, the resolidification velocity, v_r, and the melt duration, t_m.

the least known parameters. The general triangular shape of the interface dynamics does not change over the range of parameters we are interested in. All profiles are well described by melt depth, time to melt, melt duration, solidification velocity. There are experimental bounds on these characteristics. We would like to find the range of laser fluence, P_{flux}, and nonlinear absorption coefficients, β which produce melting dynamics within our experimental bounds.

Given the constraints on melt depth, $30 < x_m < 80$ nm, and solidification velocity, $v_r < 15\ \frac{m}{s}$, as well as the fact that the solidification velocity is approximately constant, we can set a lower bound for the melt duration. If the

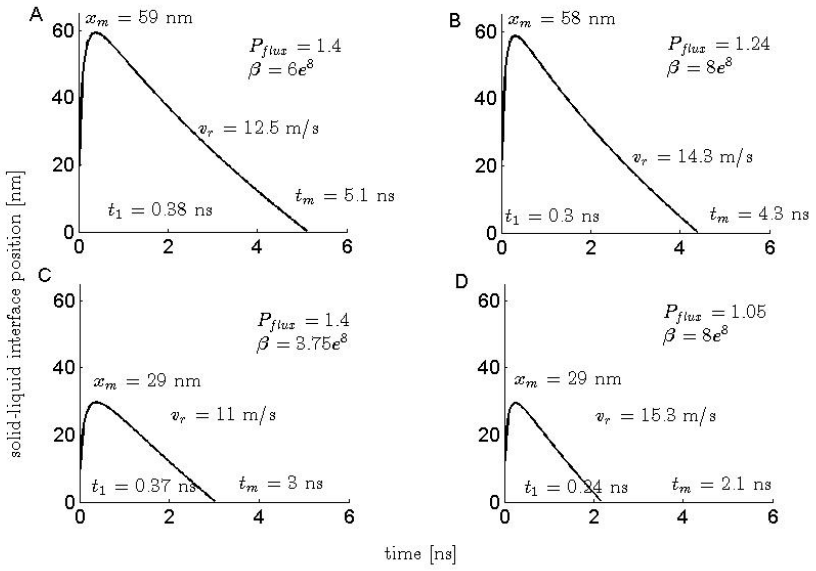

Figure 2.4.6: Interface dynamics for various combinations of laser fluence, P_{flux}, and nonlinear absorption coefficients, β. Other parameters are held fixed and are well known, see table 2.2.1. We obtain a variety of solid-liquid interface dynamics, all of which are well characterized by melt depth, solidification velocity, time to melt, and melt duration.

melt depth is 60 nm then the duration must be larger than 4 ns. Preliminary experiments in the Mazur group on the melt dynamics put an upper limit on the melt duration of 8 ns, giving us a range of $4 < t_m < 8$ ns, [unpublished data]. These measurements have about 3 ns lag time due to the delay response of the detector, it is likely that the melt duration is close to 5 ns. If the melt depth is shorter, then the lower bound can be smaller. For 30 nm melt depth the lower bound would be 2 ns.

We numerically solve the equations over a range of nonlinear absorption and laser fluence, Fig. 2.4.7. We pick pairs of values of nonlinear absorption coefficients and laser fluences which result in melt depths of 30, 40, 50, and 60 nm. We then calculate the melt depth and solidification velocity for each parameter pair, as shown in Fig. 2.4.7. We find that the experimental constraints on melt depth, solidification velocity, and melt duration constrain which pairs are reasonable. The experimental constraints are marked as gray lines in Fig. 2.4.7 marking $v_r = 15\ \frac{m}{s}$ and time to resolidify 5 ns. If the melting dynamics are not varying from shot to shot, we expect the melting dynamics resulting in $x_m \approx 60\ nm$, since sulfur is observed at least that deep in the material. Notably, this would result in a range of possible solidification velocities from $12 < v_r < 15\ \frac{m}{s}$ as shown in Fig.2.4.7 (the range of resolidification velocities at 60 nm melt depth between red dot and blue star). If we also assume that the material actually absorbs 60% of the fluence then the best parameters are $P_{flux} = 1.4\frac{kJ}{m^2}$ and $\beta = 5.6e^{8}\frac{mfs}{kJ}$, resulting in a 60 nm melt depth with a solidification velocity of 12 $\frac{m}{s}$ and around 5 ns melt duration (red dot at 60 nm melt depth in Fig. 2.4.7).

If the melting dynamics are varying from shot to shot, we find that a change in the nonlinear absorption coefficient of about 35% will increase the melt depth from 30 to 60 nm (see range of β values in Fig. 2.4.7). It is possible that either the implanted sulfur or some physical change to the material would increase the silicon's absorption after laser irradiation.

There is evidence that melting is non-thermal for fs-laser melting at these

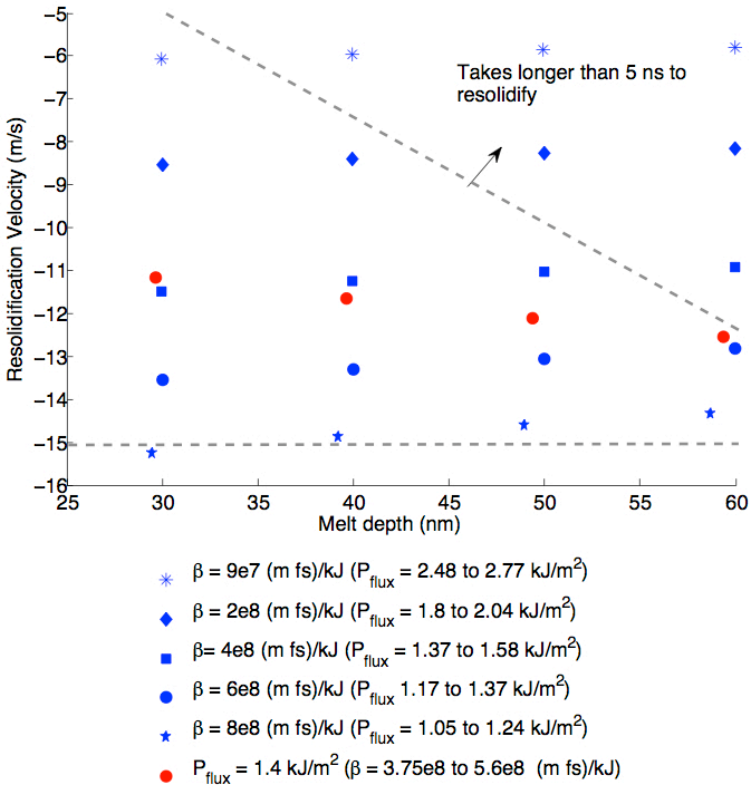

Figure 2.4.7: Melt depth and solidification velocity resulting from various β and P_{flux} values. The solidification velocity must be, $v_r < 15\frac{m}{s}$ and the melt duration is bounded by $4ns < t_m < 8ns$ and is most likely, $t_m < 5ns$. Therefore we have a range β and P_{flux} values which will give different velocities, and melt duration, but produce the same melt depth. If we assume 40% reflection of a experimental fluence $P_{flux} = 2.4$, we can find the range of nonlinear absorption, β, needed to produce 30, 40, 50, and 60 nm melt depths (red dots).

fluences [48, 52]. Non-thermal melting would mean that instead of melting from the surface, there would be homogeneous melting throughout some region of the material on the time scale of picoseconds. While we do not know how this would effect the dynamics, it would definitely shorten the time to melt to much less than the 0.5 ns it takes in our simulation. Assuming it does not affect the temperature profile outside the melted region much, especially since the non-thermal melting happens on such a short time scale. There is a possibility that the solidfication would be unaffected. The result would be an more sharply triangular melting dynamic than is seen in Fig. 2.4.5.

Given that we have a better idea of the range of the unknown parameter, β, from this study, we investigate the solute dynamics.

2.5 Solute Dynamics

When the silicon is liquid, sulfur can diffuse within the silicon. The melting dynamics set the size of the liquid region over time. The longer a region is liquid, the more time the sulfur has to diffuse and equilibrate within the region. Since the material near the surface is molten the longest, sulfur will have a longer effective diffusion time near the surface than deeper into the material. Consequently, the solute dynamics are more complicated than simple diffusion during the melt duration. The dynamics will be even further complicated if the melting dynamics vary from shot to shot.

The mechanism by which an adsorbed layer of sulfur will enter the material is unknown. We examine the two simplest assumptions. The adsorbed layer could act as a sharp initial condition described in equation 2.12, such that it all enters the material in a single dose which we call "instant dose." Instead of all getting in at $t = 0$, the layer could take time to diffuse into the material and enter as a flux. We assume it would act as a constant flux. Last of all, it could be some combination of the two. We compare the concentration profile where the total dose of sulfur integrated into silicon comes from the instant dose in the initial

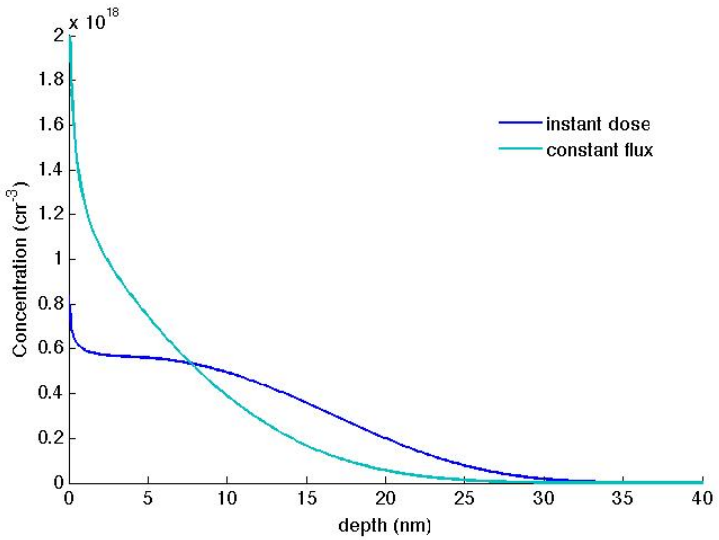

Figure 2.5.1: Single shot simulation at $P_{flux} = 1.4[\frac{kJ}{m^2}]$, and nonlinear absorption coefficient, $\beta = 6e^8[\frac{m\,fs}{kJ}]$. We either assume an instant dose is contained in the intial condition with no flux boundary condition (dark blue) or assume no dose in the initial condition and a constant flux (light blue). Both concentration profiles contain the same integrated dose.

condition (with no flux boundary condition) to a profile where the total dose comes from a constant flux at the boundary (with zero intial concentation) in Fig. 2.5.1. The profiles have distinctively different appearances. The constant flux curve is much higher at the surface, since sulfur entering near the end of solidification does not have time to diffuse into the material. For the instant dose curve, all sulfur enters at time. As a result, there is much more sulfur early on and it penetrates farther into the silicon. The instant dose curve is much flatter between 2 and 10 nm, then 20 and 30 nm, since it has more time to diffuse near the surface.

The sharp upturn at the surface is more visible in the instant dose curve, but present in both curves. The upturn comes from sulfur being rejected from the solid phase as the silicon solidifies. It cannot escape out of the silicon entirely, and piles up as the interface approaches the surface. This characteristic is visible in the higher pulses of experimental data, Fig. 2.1.2. If we increase the diffusive velocity, v_D, which sets how quickly the sulfur can diffuse away from the front, we see an increase in the rejected sulfur (Fig. 2.5.2). We simulate the concentration dynamics for doses already implanted in a material undergoing multiple shots. For example in Fig. 2.5.3, we simulate an instant dose in the first shot followed by 5 more shots with no new sulfur. During the subsequent shots, the dose from the first shot diffuses further into the material. We investigate the change in sulfur profiles if the melting dynamics are not constant between shots, Fig 2.5.4. If the melt depth increase, due to increased absorption for instance, the shape of the profile changes from a sharp looking exponential to the profile we have seen previously. The sharp profile only happens when the melt duration is very short. To achieve a melt duration short enough to prevent the formation of a plateau, the time to melt much be much smaller than is predicted by the heterogeneous, thermal melting from the surface. Therefore, in order for a short melt depth and duration to be responsible for the exponential looking profiles at low shot number, the melting would have to be non-thermal.

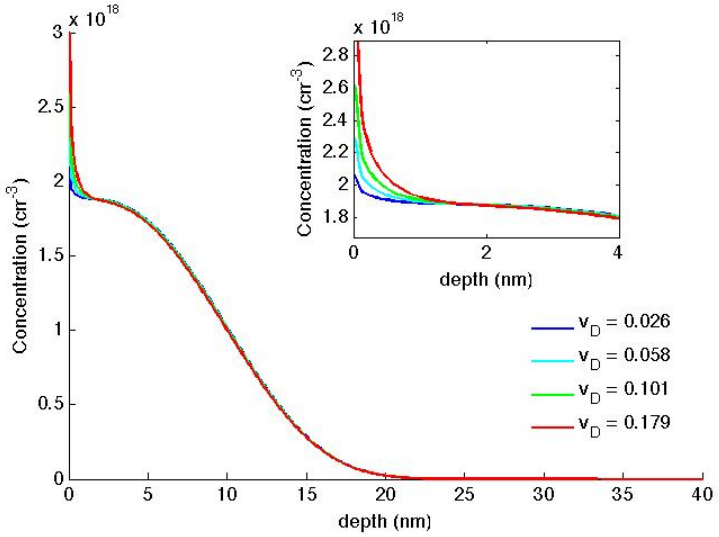

Figure 2.5.2: Single shot simulations with varying diffusive velocity, v_D. As v_D increases the solute rejection increases creating a larger upturn at the surface. Melting dynamics are set by $P_{flux} = 1.5[\frac{kJ}{m^2}]$, and nonlinear absorption coefficient, $\beta = 3.38e^8[\frac{m\,fs}{kJ}]$. We either assume an instant dose is contained in the initial condition. All profiles have the same total dose.

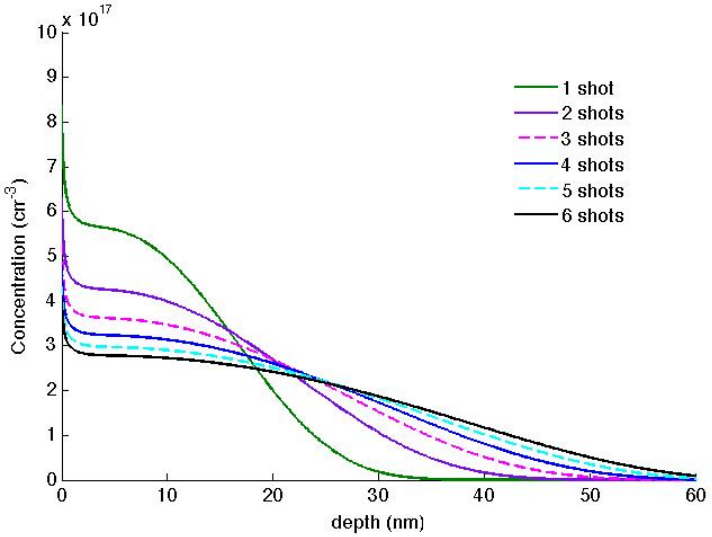

Figure 2.5.3: Multiple shot simulations with a single instant dose on entering on the first shot. Melting dynamics are set by$P_{flux} = 1.4[\frac{kJ}{m^2}]$, and nonlinear absorption coefficient, $\beta = 6e^8[\frac{m\,fs}{kJ}]$.

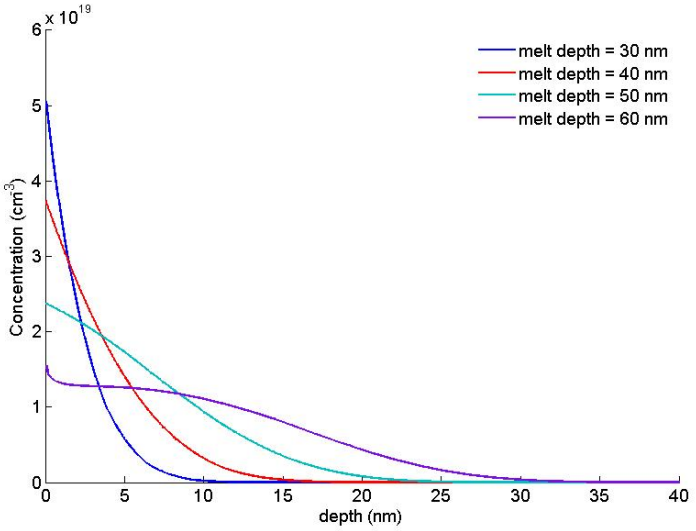

Figure 2.5.4: Concentration profiles for increasing melt depth. Simulated by solving the solute diffusion only, where the melt dynamics are assumed to be a triangular profile with instantaneous melting, varying melt depth, and fixed solidification velocity of $v_r = 15\frac{m}{s}$.

We need to determine the mechanism for solute incorporation which accounts for all the characteristics of the solute profiles with varying pressure and shot number. At high pressure the shape of the solute profile changes quite dramatically with increasing shots. The profile changes from a smooth exponential to a plateau. As we have just shown there are two main mechanisms for changing the diffusion profiles, one is changing the melt duration and depth and the second is by changing the method by which the sulfur is incorporated into the material.

2.6 Comparison to experimental data

2.6.1 Hypothesis 1 : the melt depth changes as a function of shots

If we assume that the dose gets in as an "instant dose," or a sharp initial condition with no flux at the boundary, then for very short melt durations ($\tau_m \approx 2$ ns), we get sharp exponential curves (See the first pulse from simulation in Fig. 2.6.1). We have fit, by eye, simulations similar to those in Fig. 2.5.4 to the experimental concentration profiles in Fig. 2.6.1. The fit is done by rescaling the concentration profile. Since the concentration is linear, this is the equivalent of fitting the total dose. Each simulation is only one shot, but the experimental data is actually for multiple shots. The discrepancy in the penetration depth would be corrected by simulating all six shots. The behavior near the surface, which is the behavior we are most interested in, will not change much when all shots are done correctly. The last shot dominates the curve shape near the surface, since sulfur from previous shots then diffuses further in.

2.6.2 Hypothesis 2 : dose comes from instant dose or fluence

The second mechanism which will produce a transition from exponential curve to plateau is if the dose incorporation mechanism changed from instant dose to

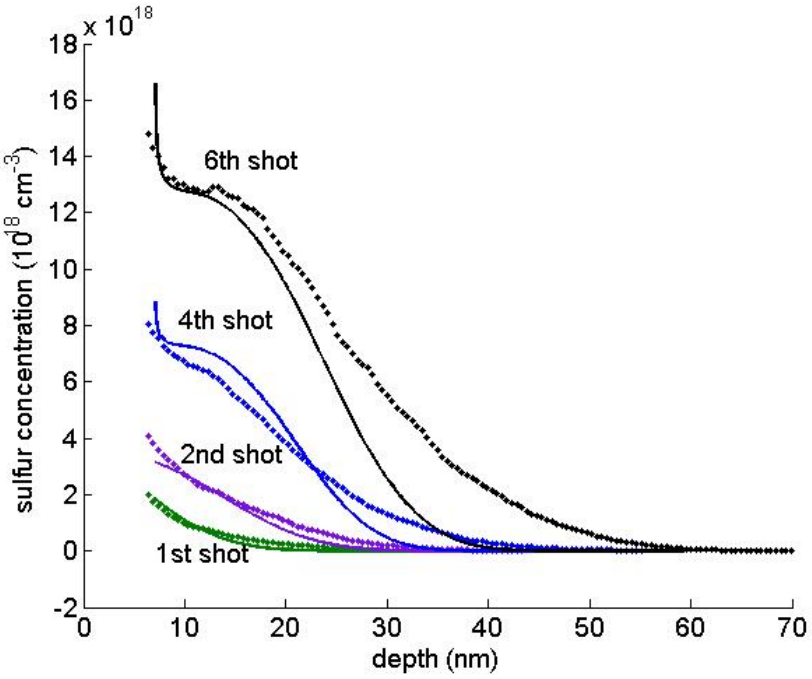

Figure 2.6.1: Dots are SIMS data giving the concentration profiles resulting from laser irradiation at $P = 500$ torr with 1, 2, 4, and 6 laser pulses at $2.5\frac{kJ}{m^2}$ laser fluence. Lines are simulations with an instant dose as the initial condition and verying melt depth. The simulations only simulate the solute dynamics and assume a triangular melt profile with negligible melting time, a solidification velocity of $\frac{m}{s}$ and a melt depth of 30, 40, 60 and 70 nm. We rescale the simulation to match the dose of the experiment. Since each simulation is only one shot, the length scale on these curves is incorrect.Since the shape of the curve at the surface is mostly determined by the dose coming in from the most recent shot, a single shot explains the behavior near the surface.

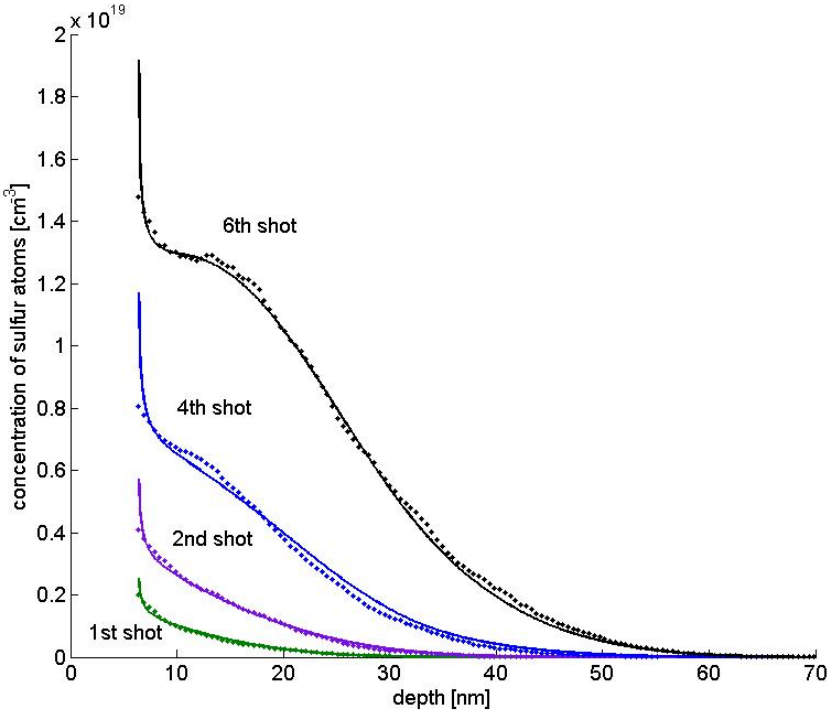

Figure 2.6.2: Fit of surface flux and instant dose to match SIMS concentration profiles for shots 1, 2, 4, and 6 at 500 torr. Percentage of dose entered by flux and instant dose are found by fitting simulations of an instant dose and constant flux experiencing 1 to 6 shots of laser irradiation, where the magnitude of the constant flux and instant dose are free parameters to be fitted.

flux. For simplicity we assume the melting dynamics are not changing. The question is then, how much instant dose and how much flux is required to fit the experimental data?

We assume that the dose is integrated into the material through a combination of "instant dose" in the initial condition and a constant flux boundary condition. We fit the concentration profiles for 1, 2, 4, and 6 shots by allowing the contribution from the initial condition and boundary condition to vary in Fig. 2.6.2. We report the percentage contributing from each for these fits in Table 2.6.1, as well as the total dose coming in from that shot. Since there is uncertainty

Table 2.6.1: Total dose of sulfur incorporated into silicon with each shot are shown. Percentage of dose entered by flux and instant dose are found by fitting simulations of an instant dose and constant flux experiencing 1 to 6 shots of laser irradiation, where the magnitude of the constant flux and instant dose are free parameters to be fitted. The error bars are calculated by starting our fitting search from a couple different initial conditions.

Shot	1	2	4	6
Total dose since last data (in $10^{12} cm^{-2}$)	1.15 ± 0.02	2.56 ± 0.06	7.83 ± 0.01	16.0 ± 0.1
Percentage entered by a flux	$100 \pm 0\%$	$94.6 \pm 2.2\%$	$42.3 - 12.1 + 7.3\%$	$0 - 0 + 0.7\%$
Percentage entered by an instant dose	$0 \pm 0\%$	$5.4 \pm 2.2\%$	$57.7 - 7.3 + 12.1\%$	$100 - 0.7 + 0\%$

in the fluence and nonlinear absorption coefficient we use the range of values found to produce a 60 *nm* melt depth. The range of selected parameters results in a change in the solidification velocity from 12 to $14 \frac{m}{s}$. Over this range, the proportion of surface flux to instant dose found from a fitting varies very little, following the same trend no mater the solidification velocity, Fig. 2.6.3. We also fit data for low pressure, Fig. 2.6.5. We compare this to a simulation where we fit the first dose of pressure, and allow dose to diffuse with subsequent shots, but add no additional dose, Fig. 2.6.4. For low pressure, the concentration in the material is low enough that contamination from the surface could be distorting the SIMS data for the first few nm.

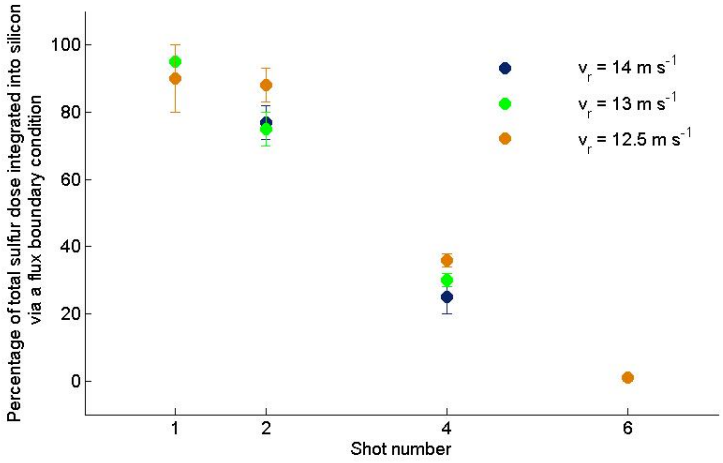

Figure 2.6.3: We vary the laser fluence and nonlinear absorption coefficient to analyze the effect a varying solidification velocity has on the solute dynamics, and conduct a fitting of the instant dose and constant flux. Here is the percentage of dose coming from a flux boundary condition, with error bars determined by fitting using multiple initial guesses for the fitting. The melt depth for all data is chosen to be 60 nm. For the $v_r = 14\frac{m}{s}$ data, $\beta = 8e^8$ and $P_{flux} = 1.24\frac{kJ}{m^{-2}}$. For $v_r = 13\frac{m}{s}$ data, $\beta = 6.9e^8$ and $P_{flux} = 1.3\frac{kJ}{m^{-2}}$. For the $v_r = 12.5\frac{m}{s}$ data, $\beta = 5.7e^8$ and $P_{flux} = 1.4\frac{kJ}{m^{-2}}$.

Table 2.6.2: Table of flux fit percentages for low pressure regime. Fig. 2.6.5

Shot	1	2	4	6
Total dose since last data (in $10^{12}cm^{-2}$)	0.53 ± 0.09	0.15 ± 0.3	0.1 ± 0.1	0.1 ± 0.1
Percentage entered by a flux	$95 \pm 5\%$	$90 \pm 10\%$	$95 \pm 5\%$	$95 \pm 5\%$

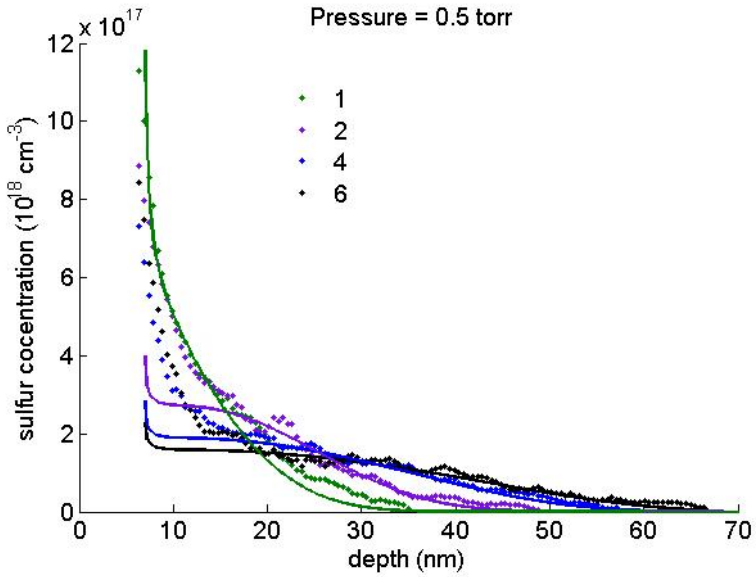

Figure 2.6.4: Dots are SIMS data giving the concentration profiles resulting from laser irradiation at $P = 0.5$ *torr* with 1, 2, 4, and 6 laser pulses at $2.5\frac{kJ}{m^2}$ laser fluence. Lines are simulations with a dose coming from surface flux at the first shot with no incoming sulfur during subsequent shots. The melting dynamics are constant between shots with simulation fluence is $P_{flux} = 1.4\frac{kJ}{m^2}$ and nonlinear absorption coefficient is $\beta = 5.6 \times 10^8 \frac{m\,fs}{kJ}$. To match the simulation to the experiment we scale the first shot of the simulation to match the dose from the experiment. We also shift the simulation data by 7 nm to roughly account for the SIMS push down effect and surface oxide layer.

2.7 Discussion

With current data we are unable to distinguish between the two mechanisms for changing concentration profile. Future experiments could differentiate between the two mechanisms for changing profile shape, by determining if the actual melt dynamics are changing between laser shots. If changes in melt depth are responsible for the profile change, the simulations indicate that the melt depth would have to change by 30 nm and the melt duration would have to change by 3 ns to create the change in profile observed. A pump-probe experiment probing the position of the solid-liquid interface could distinguish these time and length

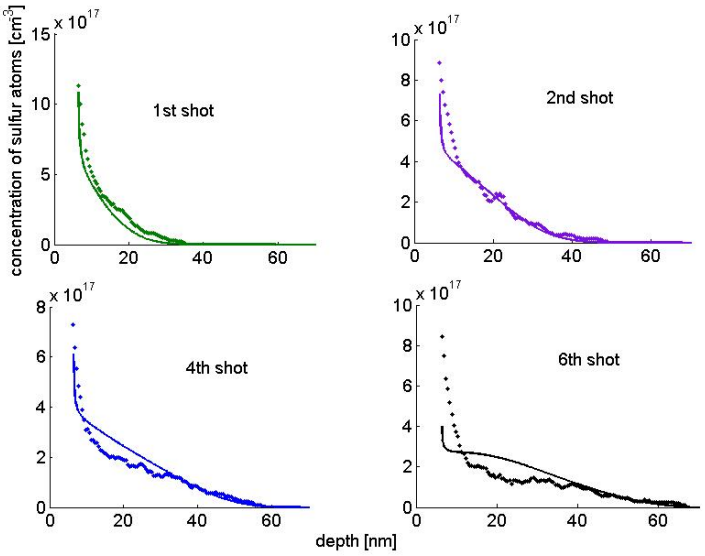

Figure 2.6.5: Dots are SIMS data giving the concentration profiles resulting from laser irradiation at $P = 0.5\ torr$ with 1, 2, 4, and 6 laser pulses at $2.5\frac{kJ}{m^2}$ laser fluence. The melting dynamics are constant between shots with simulation fluence is $P_{flux} = 1.4\frac{kJ}{m^2}$ and nonlinear absorption coefficient is $\beta = 5.6 \times 10^8 \frac{m\,fs}{kJ}$. Percentage of dose entered by flux and instant dose are found by fitting simulations of an instant dose and constant flux experiencing 1 to 6 shots of laser irradiation, where the magnitude of the constant flux and instant dose are free parameters to be fitted. We also shift the simulation data by $7\ nm$ to roughly account for the SIMS push down effect and surface oxide layer.

scales. It could also clarify whether the melting is thermal or non-thermal. If the melting is non-thermal then the model could be altered to assume homogenous melting across some region. However, unlike melting from the surface, choosing the thermal distribution as an initial condition with homogeneous melting is non trivial. Pump-probe experiments could help determine whether a triangular description of the melt dynamics with very fast melting and constant solidification is accurate.

If the melting dynamics are not changing, but the level of surface flux and instant dose are, there must be physical explanation. We propose that the silicon

oxide layer, which develops on the surface of silicon when exposed to air, could be responsible for the change in mechanism for sulfur incorporation over shot number. As Table 2.6.1 shows there is a fairly smooth transition between constant flux and instant dose as the main component incorporating the dose into the material. For the first few shots, the sulfur has to diffuse through the oxide layer to get into silicon creating a flux at the surface. With increasing shots, the oxide is blasted away, allowing more and more sulfur to get in as a instant dose. If this is the case, removing the oxide layer prior to laser irradiation would introduce the entire dose as a instant dose and there would be no transition with subsequent laser pulses.

References

[1] M. M. Allen. Cyanobacterial cell inclusions. *Ann. Rev. Microbiol.*, 38:1–25, 1984. http://dx.doi.org/10.1146/annurev.mi.38.100184.000245.

[2] M. J. Aziz and T. Kaplan. Continuous growth model for interface motion during alloy solidification. *Acta metallurgica*, 36:2335–2347, 1988. http://dx.doi.org/10.1016/0001-6160(88)90333-1.

[3] M. J. Aziz and C. W. White. Solute trapping in silicon by lateral motion of {111} ledges. *Physical Review Letters*, 57:2675–2678, 1986. http://dx.doi.org/10.1103/PhysRevLett.57.2675.

[4] M. R. Badger and G. D. Price. CO_2 concentrating mechanisms in cyanobacteria: molecular components and their diversity and evolution. *Journal of Exp. Bot.*, 54:609–622, 2003. http://dx.doi.org/10.1093/jxb/erg076.

[5] M. R. Badger, M. Bassett, and H. N. Comins. A model for HCO_3^- accumulation and photosynthesis in the cyanobacterium S*ynechococcus* sp.: theoretical predictions and experimental observations. *Plant Physiol.*, 77, 1985. http://dx.doi.org/ 10. 1104/ pp. 77. 2. 465.

[6] M. A. Bassam, P. Parvin, B. Sajad, A. Moghimi, and H. Coster. Measurement of optical and electrical properties of silicon microstructuring induced by arf excimer laser at sf6 atmosphere. *Applied Surface Science*, 254:2621–2628, 2008. http://dx.doi.org/10.1016/j.apsusc.2007.09.106.

[7] G. G. Bentini, M. Bianconi, L. Correra, R. Nipoti, D. A. Patti, and A. Gasparotto. Laser doping of silicon role of the surface status in the incorporation mechanism. *Applied Surface Science*, 36:394–399, 1989. http://dx.doi.org/10.1016/0169-4332(89)90934-3.

[8] B. P. Bob, A. Kohno, S. Charnvanichborikarn, J. M. Warrender, I. Umezu, M. Tabbal, J. S. Williams, and M. J. Aziz. Fabrication and subband gap optical properties of silicon supersaturated with chalcogens by ion implantation and pulsed laser melting. *Journal of Applied Physics*, 107: 123506, 2010. http://dx.doi.org/10.1063/1.3415544.

[9] P. M. Boyle C. M. Agapakis and P. A. Silver. Natural strategies for the spatial optimization of metabolism in synthetic biology. *Nature Chem. Bio.*, 8:527–535, 2012. http://dx.doi.org/10.1038/nchembio.975.

[10] G. C. Cannon, R.S. English, and J. M. Shively. In situ assay of ribulose-1,5-bisphosphate carboxylase/oxygenase in thiobacillus neapolitanus. *J. Bacteriol.*, 173:1565–1568, 1991. http://jb.asm.org/content/173/4/1565.long.

[11] G. C. Cannon, C. E. Bradburne, H. C. Aldrich, S. H. Baker, S. Heinhorst, and J. M. Shively. Microcompartments in prokaryotes: Carboxysomes and related polyhedra. *Appl. Environ. Microbiol.*, 67:5351–5361, 2001. http://dx.doi.org/10.1128/AEM.67.12.5351-5361.2001.

[12] S. Cheng, Y. Liu, C. S. Crowley, T. O. Yeates, and T. A. Bobik. Bacterial microcompartments: their properties and paradoxes. *Bio Essays*, 30: 1084–1095, 2008. http://dx.doi.org/10.1002/bies.20830.

[13] M. Chibata, H. Ohkawa, T. Kaneko, H. Fukuzawa, S. Tabata, A. Kaplan, and T. Ogawa. Distinct constitutive and low-co_2-induced co_2 uptake systems in cyanobacteria: genes involved and their phylogenetic relationship with homologous genes in other organisms. *PNAS.*, 98: 11789–11794, 2001. http://dx.doi.org/10.1073/pnas.191258298.

[14] S.S. Cot, A. K. So, and G. S. Espie. A multiprotein bicarbonate dehydration complex essential to carboxysome function in cyanobacteria. *J. Bacteriol.*, 190:936–945, 2008. http://dx.doi.org/10.1128/JB.01283-07.

[15] C. H. Crouch, J. E. Carey, J. M. Warrender, M. J. Aziz, E. Mazur, and F. Y. Genin. Comparison of structure and properties of femtosecond and nanosecond laser structured silicon. *App. Phys. Lett.*, 84:1850, 2004. http://dx.doi.org/10.1063/1.1667004.

[16] H. DeVoe and G. B. Kistiakowsky. The enzymatic kinetics of carbonic anhydrase from bovine and human erythrocytes. *Journal of the American Chemical Society*, 83:274–280, 1961. http://dx.doi.org/10.1021/ja01463a004.

[17] Z. Dou, S. Heinhorst, E. B. Williams, C. D. Murin, and J. M. Shively. CO_2 fixation kinetics of hlothiobacilus neapolitanus mutant carboxysomes lacking carbonic anhydrase suggest the shell acts as a diffusional barrier for co2. *J. Biol. Chem.*, 283:10377–10384, 2008. http://dx.doi.org/10.1074/jbc.M709285200.

[18] D.C. Ducat and P.A. Silver. Improving carbon fixation pathways. *Current Opinion in Chem. Bio.*, 16:337–344, 2012. http://dx.doi.org/10.1016/j.cbpa.2012.05.002.

[19] J. Gutknecht, M. A. Bisson, and F. C. Tosteson. Diffusion of carbon dioxide through lipid bilayer membranes: effects of carbonic anyhdrase, bicarbonate, and unstirred layers. *The J. of Gen. Physiol.*, 69:779–794, 1977. http://dx.doi.org/10.1085/jgp.69.6.779.

[20] S. Heinhorst, E. B. Williams, R. Cai, C. D. Murin, J. M. Shively, and G. C. Cannon. Characterization of the carboxysomal carbonic anhydrase CsoSCA from *halothiobacillus neapolitanus*. *J. of Bacteriology*, 188, 2006. http://dx.doi.org/10.1128/JB.00990-06.

[21] D. E. Hoglund, M. O. Thompson, and M. J. Aziz. Experimental test of morphological stability for a planar interface during rapid solidification. *Phys. Rev. B*, 58:189–199, 1998. http://dx.doi.org/10.1103/PhysRevB.58.189.

[22] D.A. Huntley and S. H. Davis. Thermal effects in rapid directional solidification: linear theory. *Acta metallurgica*, 41:2025–2043, 1993. http://dx.doi.org/10.1016/0956-7151(93)90373-Z.

[23] D. B. Jordan and W. L. Ogren. Species variation in the specificity of ribulose bisphosphate carboxylase/oxygenase. *Nature*, 291, 1981. http://dx.doi.org/10.1038/291513a0.

[24] A. Kaplan and L. Reinhold. CO_2 concentrating mechanisms in photosynthetic microorganisms. *Ann. Rev. Plant Physiol. Plant Mol. Biol.*,

50:539–570, 1999.
http://dx.doi.org/10.1146/annurev.arplant.50.1.539.

[25] T. Kim, M. R. Pillai, M. J. Aziz, M. A Scarpulla, O. D. Dubon, K. M. Yu, J. W. Beeman, and M. C. Ridgeway. Heat flow model for pulsed laser melting and rapid solidification of ion implanted GaAs. *J. App. Phys.*, 108: 013508, 2010. http://dx.doi.org/10.1063/1.3457106.

[26] J. A. Kittl, P. G. Sanders, M. J. Aziz, D. P. Brunco, and M. O. Thompson. Complete experimental test of kinetic models for rapid alloy solidification. *Acta Materialia*, 48:4797–4811, 2000.
http://dx.doi.org/10.1016/S1359-6454(00)00276-7.

[27] D. P. Korfiatis, K-A. Th. Thoma, and J. C. Vardaxoglou. Conditions for femtosecond laser melting of silicon. *J Phys. D: Appl. Phys*, 40:6803–6808, 2007. http://dx.doi.org/10.1088/0022-3727/40/21/047.

[28] Y. Liu, S. Liu, Y. Wang, G. Feng, J. Zhu, and L. Zhao. Broad band enhanced infrared light absorption of a femtosecond laser microstructured silicon. *Laser Physics*, 18:1148–1152, 2008.
http://dx.doi.org/10.1134/S1054660X08100071.

[29] B. M. Long, M. R. Badger, S. M. Whitney, and G. D. Price. Analysis of carboxysomes from *synechococcus* PCC7942 reveals multiple rubisco complexes with carboxysomal proteins CcmM and CcaA. *J. Biol. Chem.*, 292:29323–29335, 2008.
http://dx.doi.org/10.1074/jbc.M703896200.

[30] A. Luque and A. Mari. The intermediate band solar cell: progress toward teh realization of an attractive concept. *Adv. Mat.*, 22:160–174, 2010.
http://dx.doi.org/10.1002/adma.200902388.

[31] S. Maeda, M. R. Badger, and G. D. Price. Novel gene products associated with NdhD3/D4-containing NDH-1 complexes are involved in photosynthetic co_2 hydration in the cyanobacterium, *synechococcus* sp. strain PCC7942. *Molecular Microbiol.*, 43:425–435, 2002.
http://dx.doi.org/10.1046/j.1365-2958.2002.02753.x.

[32] A. Missner, P. Kügler, S. M. Saparov, K. Sommer, J. C. Mathai, M. L. Zeide, and P. Pohl. Carbon dioxide transport through membranes. *J. Biol. Chem.*,

283:25340–25347, 2008.
http://dx.doi.org/10.1074/jbc.M800096200.

[33] T. Omata, G.D. Price, M. R Badger, M Okamura, S. Gohta, and T. Ogawa. Identification of an ATP-binding cassette transporter involved in bicarbonate uptake in the cyanobacterium *synechococcus* sp strain PCC7942. *PNAS*, 96:13571–13576, 1999. http://dx.doi.org/10.1073/pnas.96.23.13571.

[34] D. Papapostolou and S. Howorka. Engineering and exploiting protein assemblies in synthetic biology. *Molecular BioSystems*, 5:723–732, 2009. http://dx.doi.org/10.1039/B902440A.

[35] M. U. Pralle, J.E. Carey, H. Homayoon, S. Alie, J. Sickler adn X. Li, J. Jiang, D. Miller, C. Palsule, and J. McKee. Black silicon enhanced photodetectors: a path to IR CMOS. In *Proc. SPIE7600: Infrared Technology and Applications XXXVI*, volume 76600N, May 2010. http://dx.doi.org/10.1117/12.849683.

[36] G. D. Price, D. Sultemeyer, B. Klughammer, M. Ludwig, and M. R. Badger. The functioning of the co_2 concentrating mechanism in several cyanobacterial strains: a review of general physiological characteristics, genes, proteins, and recent advances. *Canadian J. Botany*, 76:973–1001, 1998. http://dx.doi.org/10.1139/b98-081.

[37] G. D. Price, F. J. Woodger, M. R. Badger, S. M. Howitt, and L. Tucker. Identification of a SuIP-type bicarbonate transporter in marine cyanobacteria. *PNAS*, 101:18228–18233, 2004. http://dx.doi.org/10.1073/pnas.0405211101.

[38] G. D. Price, M. R. Badger, F. J. Woodger, and B. M. Long. Advances in understanding the cyanobacterial CO2-concentrating-mechanism (CCM): functional components, C_i transporters, diversity, genetic regulation and prospects for engineering into plants. *J. Exp. Botany*, 58: 1441–1461, 2007. http://dx.doi.org/10.1093/jxb/erm112.

[39] G. D. Price, M. R. Badger, F. J. Woodger, and B. M. Long. Advances in understanding the cyanobacterial co_2-concentrating-mechanism (ccm): functional components, c_i transporters, diversity, genetic regulation and prospects for engineering into plants. *J. Exp. Botany.*, 59:1441–1461, 2008. http://dx.doi.org/10.1093/jxb/erm112.

[40] G.D. Price and M. R. Badger. Expression of human carbonic anhydrase in the cyanobacterium *Synechococcus* PCC7942 creates a high CO_2-requiring phenotype. *Plant Physiol.*, 91:505–513, 1989. http://dx.doi.org/10.1104/pp.91.2.505.

[41] L. Reinhold, R. Kosloff, and A. Kaplan. A model for inorganic carbon fluxes and photosynthesis in cyanobacterial carboxysomes. *Can. J. Bot.*, 69: 984 – 988, 1991. http://dx.doi.org/10.1139/b91-126.

[42] R. Reitano, P. M. Smith, and M. J. Aziz. Solute trapping of group iii, iv, and v elements in silicon by an aperiodic stepwise growth mechanism. *Journal of Applied Physics*, 76:1518–1529, 1994. http://dx.doi.org/10.1063/1.357728.

[43] L. Ridlyand, A. Kaplan, and L. Reinhold. Quantitative evaluation of the role of a putative CO_2-scavenging entity in the cyanobacterial CO_2-concentrating mechanism. *BioSystems*, 37:229–238, 1996. http://dx.doi.org/10.1016/0303-2647(95)01561-2.

[44] L. Rosgaard, A. J. de Porcellinis adn J. H. Jacobsen, N. U. Frigaard, and Y. Sakuragi. Bioengineering of carbon fixation, biofuels, and biochemcials in cyanobacteria and plants. *Journal of Biotechnology*, 162:137–147, 2012. http://dx.doi.org/10.1016/j.jbiotec.2012.05.006.

[45] D. F. Savage, B. Alfonso, A. Chen, and P. A. Silver. Spatially ordered dynamics of the bacterial carbon fixation machinery. *Science*, 327: 1258–1261, 2010. http://dx.doi.org/10.1126/science.1186090.

[46] Y. Savir, E. Noor, R. Milo, and T. Tlusty. Cross-species analysis traces adaptation of rubisco toward optimality in a low-dimensional landscape. *PNAS*, 107:3475–3480, 2010. http.//dx.doi.org/10.1073/pnas.0911663107.

[47] M. F. Schmid, A. M. Paredes, H. A. Khant, F. Soyer, H. C. Aldrich, W. Chiu, and J. M. Shively. Structure of halothiobacillus neapolitanus carboxysomes by cryo-electron tomography. *J. Mol. Biol.*, 364:526–535, 2006. http://dx.doi.org/10.1016/j.jmb.2006.09.024.

[48] C. V. Shank, R. Yen, and C. Hirlimann. Time-resolved reflectivity measurements of femtosecond-optical-pulse-induced phase transitions in

silicon. *Phys. Rev. Lett.*, 50:454–457, 1983. http://dx.doi.org/10.1103/PhysRevLett.50.454.

[49] M. Sher. *Intermediate Band Properties of Femtosecond-Laser Hyperdoped Silicon*. PhD thesis, Harvard University, 2013. http://mazur-www.harvard.edu/publications.php?function=display&rowid=704.

[50] A. Slaoui, F. Foulon, and P. Siffert. Excimer laser induced doping of phosphorus into silicon. *Journal of Applied Physics*, 67:6197–6201, 1990. http://dx.doi.org/10.1063/1.345186.

[51] M. J. Smith, M.-J. Sher, B. Franta, Y.-T. Lin, E. Mazur, and S. Gradecak. Response to "comment on 'the origins of pressure-induced phase transitions during the surface texturing of silicon using femtosecond laser irradiation' ". *Journal of Applied Physics*, 113:126103, 2013. http://dx.doi.org/10.1063/1.4796126.

[52] K. Sokolowski-Tinten and D. v.d. Linde. Ultrafast phase transitions and lattice dynamics probed using laer-produced x-ray pulses. *J. Phys.: Condens. Matter*, 16:1517–1536, 2004. http://dx.doi.org/10.1088/0953-8984/16/49/R04.

[53] P. A. Stolk, A. Polman, and W. C. Sinke. Experimental test of kinetic theories for hetergeneous freezing in silicon. *Phys. Rev. B*, 47:5–13, 1993. http://dx.doi.org/10.1103/PhysRevB.47.5.

[54] D. Recht J. T. Sullivan, R. Reedy, T. Buonassisi, and M. J. Aziz. Controlling dopant profiles in hyperdoped silicon by modifying dopant evaporation rates during pulsed laser melting. *App. Phys. Lett.*, 100:112112 1–3, 2012. http://dx.doi.org/10.1063/1.3695171.

[55] D. Sultemeyer, G. D. Price, J-W. Yu, and M. R. Badger. Characterisation of carbon dioxide and bicarbonate transport during steady-state photosynthesis in the marine cyanobacterium *Synechococcus* strain PCC7002. *Planta*, 197:597–607, 1995. http://dx.doi.org/10.1007/BF00191566.

[56] S. K. Sundaram and E. Mazur. Inducing and probing non-thermal transitions in semiconductors using femtosecond laser pulses. *Nature Materials*, 1:217–224, 2002. http://dx.doi.org/10.1038/nmat767.

[57] G. G. Tcherkez, G. D. Farquhar, and T. J. Andrews. Despite slow catalysis and confused substrate specificity, all ribulose bisphosphate carboxylases may be nearly optimized. *Proc. Natl. Acad. Sci. USA*, 103:7246 – 7251, 2006. http://dx.doi.org/10.1073/pnas.0600605103.

[58] M. O. Thompson, J. W. mayer, A. G. Cullis, H. C. Webber, N. G. Chew, and J. M. Poate adn D. C. Jacobson. Silicon melt, regrowth, and amorphization velocities during pulsed laser irradiation. *Phys. Rev. Lett.*, 50:896 –899, 1983. http://dx.doi.org/10.1103/PhysRevLett.50.896.

[59] Y. Tsai, M. R. Sawaya, G. C. Cannon, R. Cai, E. B. Williams, S. Heinhorst, C. A. Kerfeld, and T. O. Yeates. Structural analysis of CsoS1A and the protein shell of the *halothiobacillus neapolitanus* carboxysome. *PLOS*, 5: 1345–1354, 2007. http://dx.doi.org/10.1371/journal.pbio.0050144.

[60] B. R. Tull, J.E. Carey, E. Mazur adn J. P. McDonald, and S. M. Yalisove. Silicon surface morphologies after femtosecond laser irradiation. *MRS Bulletin*, 31:626–633, 2006. http://dx.doi.org/10.1557/mrs2006.160.

[61] C.W. White, S. R. Wilson, B. R. Appleton, and F. W. Young. Supersaturated substitutional alloys formed by ion implantation and pulsed laser annealing of group-III and group-V dopants in silicon. *J. Appl. Phys.*, 51:738, 1980. http://dx.doi.org/10.1063/1.327334.

[62] M. Winkler. *Non-equilbirium chalcogen concentrations in silicon: physical structure, electronic transport, and photovoltaic potential*. PhD thesis, Harvard University, 2009. http://mazur-www.harvard.edu/publications.php?function=display&rowid=648.

[63] M. T. Winkler, M.-J. Sher, Y.-T. Lin, M. J. Smith, S. Gradecak H. Zhang, , and E. Mazur. Studying femtosecond-laser hyperdoping by controlling surface morphology. *Journal of Applied Physics*, 111:093511, 2012. http://dx.doi.org/10.1063/1.4709752.

[64] F. J. Woodger, M. R. Badger, and G. D. Price. Sensing of inorganic carbon limitation in *Synechococcus* PCC7942 is correlated with the size of the internal inorganic carbon pool and involves oxygen. *Plant Physiol.*, 139: 1959–1969, 2005b. http://dx.doi.org/10.1104/pp.105.069146.

[65] C. Wu, C. H. Crouch, L. Zhao, J. E. Carey, R. Younkin, J. A. Levinson, E. Mazur, R. M. Farrell, P. Gothoskar, and A. Karger. Near-unity below-band-gap absorption by microstructured silicon. *Applied Physics Letters*, 78:1850–1852, 2001. http://dx.doi.org/10.1063/1.1358846.

[66] T. O. Yeates, T. Y. Tsai, S. Tanaka, and C. A. Kerfeld. Self-assembly in the carboxysome: a viral capsid-like protein shell in bacterial cells. *Biochemical Society Transactions*, 35:508 – 511, 2007. http://dx.doi.org/10.1042/BST0350508.

[67] T. O. Yeates, C. A. Kerfeld adn S. Heinhorst, Gordon C. Cannon, and J. M. Shively. Protein-based organelles in bacteria: carboxysomes and related microcompartments. *Nat. Rev. Microbiol.*, 6:681– 691, 2008. http://dx.doi.org/10.1038/nrmicro1913.

[68] V. Zorba, N. Boukos, I. Zergioti, and C. Fotakis. Ultraviolet femtosecond, picosecond and nanosecond laser microstructuring of silicon: structural and optical properties. *Applied Optics*, 47:1846–1850, 2008. http://dx.doi.org/10.1364/AO.47.001846.

A

Carbon Concentrating Mechanism Appendix

A.0.1 Full equations of CCM

$$\partial_t C = D\nabla^2 C + R_{CA} - R_{Rub} \tag{A.1}$$

$$\partial_t H = D\nabla^2 H - R_{CA}, \tag{A.2}$$

$$R_{CA}\left(H, C\right) = \frac{V_{ba}K_{ca}H - V_{ca}K_{ba}C}{K_{ba}K_{ca} + K_{ca}H + K_{ba}C} \tag{A.3}$$

$$R_{Rub} = \frac{V_{max}C}{C + K'_m(1 + \frac{O}{K_i})} \tag{A.4}$$

$$\tag{A.5}$$

$$D\frac{\partial C}{\partial r}|_{r=R_c} = k_c(C_{cytosol} - C_{carboxysome}) \tag{A.6}$$

$$D\frac{\partial H}{\partial r}|_{r=R_c} = k_c(H_{cytosol} - H_{carboxysome}). \tag{A.7}$$

$$\partial_t C = D\nabla^2 C,\ r > R_c \tag{A.8}$$

$$\partial_t H = D\nabla^2 H,\ r > R_c. \tag{A.9}$$

$$D\frac{\partial C}{\partial r}|_{r=R_b} = -\frac{aC_{cytosol}}{K_a + C_{cytosol}} + k_m^C\left(C_{out} - C_{cytosol}\right) \tag{A.10}$$

$$D\frac{\partial H}{\partial r}|_{r=R_b} = j_c H_{out} + \frac{aC_{cytosol}}{K_a + C_{cytosol}} + k_m^H\left(H_{out} - H_{cytosol}\right) \tag{A.11}$$

A.0.2 Parameters used to produce figures.

Table A.0.1: Table comparing enzymatic rates. [20, 55, 64] V_{ba} (V_{max} for carbonic anhydrase dehydration) is estimated by assuming $K_{eq} = 5$ and using parameters found in [20]

Enzyme reaction	active sites	$k_{cat}\left[\frac{1}{s}\right]$	V_{max} in 'cell' $\left[\frac{\mu M}{s}\right]$	V_{max} in carboxysome $\left[\frac{\mu M}{s}\right]$	$K_{1/2}$ $[\mu M]$
carbonic anhydrase hydration	80	8×10^4	1.1×10^4	2×10^8	3.2×10^3
carbonic anhydrase dehydration	80	4.6×10^4	9.5×10^4	1.67×10^8	9.3×10^3
RuBisCO carboxylation	2160	26	103	1.7×10^6	270

Table A.0.2: Parameter values chosen for simulations.

Parameter	Definition	Value	Reference
H_{out}	concentration of bicarbonate outside the cell	14 μM	[39]
C_{out}	concentration of carbon dioxide outside of cell dependent on pH	0.14 μM	[39]
D	diffusion constant of small molecules, CO_2 and HCO_3^-	10^{-5} $\frac{cm^2}{s}$	[43]
k_m^C	permeability of cell membrane to CO_2	0.3 $\frac{cm}{s}$	[19, 32]
k_m^H	permeability of cell membrane to HCO_3^-	$3e^{-4}$ $\frac{cm}{s}$	[19, 32]
R_c	radius of carboxysome	$5e^{-6}$ cm	[12, 47]
R_b	radius of bacteria	$5e^{-5}$ cm	[45]

A.0.3 Equations in the cytosol

The equations for diffusion of HCO_3^-, H, and CO_2, C, in the cytosol are

$$\partial_t C = D\nabla^2 C \tag{A.12}$$

$$\partial_t H = D\nabla^2 H. \tag{A.13}$$

Here D is the diffusion coefficient.

At steady state and in spherical coordinates the solutions to $\nabla^2 C = 0$ and $\nabla^2 H = 0$ are known; they have the form

$$C = \frac{A_3}{r} + A_4 \tag{A.14}$$

$$H = \frac{B_3}{r} + B_4 \tag{A.15}$$

where A_3, A_4, B_3, and B_4 are constants set by the boundary conditions.

The boundary condition at the cell membrane sets the gradient;

$$D\frac{\partial C}{\partial r} = -\frac{aC_{cytosol}}{K_a + C_{cytosol}} + k_m^C \left(C_{out} - C_{cytosol}\right) \tag{A.16}$$

$$D\frac{\partial H}{\partial r} = j_c H_{out} + \frac{aC_{cytosol}}{K_a + C_{cytosol}} + k_m^H \left(H_{out} - H_{cytosol}\right) \tag{A.17}$$

Here active transport of HCO_3^- is set by the transport velocity j_c. Conversion of CO_2 to HCO_3^- has maximum velocity a and half maximum concentration K_a. The permeability of the cell membrane to CO_2 and HCO_3^- are set by escape velocities k_m^C and k_m^H. We will assume the reactions are unsaturated, so $\frac{aC_{cytosol}}{K_a + C_{cytosol}} \approx \frac{a}{K_a} C_{cytosol}$.

Similarly the gradient at the carboxysome shell sets the linking boundary condition between the concentrations inside the carboxysome and in the cytosol.

$$D\frac{\partial C}{\partial r} = k_c(C_{cytosol} - C_{carboxysome}) \tag{A.18}$$

$$D\frac{\partial H}{\partial r} = k_c(H_{cytosol} - H_{carboxysome}). \tag{A.19}$$

Here the velocity of transport across the carboxysome shell is k_c.

Solution in cytosol

Using equation (A.14) in boundary condition (A.18) and equation (A.15) in boundary condition (A.18), we obtain:

$$A_4 = C_{carboxysome} - A_3 \left(\frac{D}{k_c R_c^2} + \frac{1}{R_C}\right) \tag{A.20}$$

$$B_4 = H_{carboxysome} - B_3 \left(\frac{D}{k_c R_c^2} + \frac{1}{R_C}\right) \tag{A.21}$$

so

$$C = A_3 \left(\frac{1}{r} - \frac{D}{k_c R_c^2} - \frac{1}{R_C}\right) + C_{carboxysome} \tag{A.22}$$

$$H = B_3 \left(\frac{1}{r} - \frac{D}{k_c R_c^2} - \frac{1}{R_C}\right) + H_{carboxysome} \tag{A.23}$$

Then using (A.22) in (A.16) and (A.23) in (A.17) we find;

$$A_3 = \frac{(\frac{a}{K_a} + k_m^C)C_{carboxysome} - k_m^C C_{out}}{(\frac{a}{K_a} + k_m^C)G + \frac{D}{R_b^2}} \tag{A.24}$$

$$B_3 = \frac{(k_m^H H_{carboxysome} - (j_c + k_m^H)H_{out} - \frac{a}{K_a}C_{cytosol}(r = R_b))}{k_m^H G + \frac{D}{R_b^2}} \tag{A.25}$$

We have grouped the following parameters:

$$G = \left(\frac{D}{R_c^2 k_c} + \frac{1}{R_c} - \frac{1}{R_b}\right) \tag{A.26}$$

Using our values for these constants, the equations for CO_2 and HCO_3^- in the cytosol are;

$$C_{cytosol} = \frac{k_m^C C_{out} - (\frac{a}{K_a} + k_m^C)C_{carboxysome}}{(\frac{a}{K_a} + k_m^C)G + \frac{D}{R_b^2}} \left(\frac{D}{k_c R_c^2} + \frac{1}{R_C} - \frac{1}{r}\right) + C_{carboxysome} \tag{A.27}$$

$$\begin{aligned} H_{cytosol} = &\frac{(j_c + k_m^H)H_{out} - k_m^H H_{carboxysome}}{k_m^H G + \frac{D}{R_b^2}} \left(\frac{D}{k_c R_c^2} + \frac{1}{R_C} - \frac{1}{r}\right) \\ &+ \frac{\frac{a}{K_a}C_{cytosol}(r = R_b)}{k_m^H G + \frac{D}{R_b^2}} \left(\frac{D}{k_c R_c^2} + \frac{1}{R_C} - \frac{1}{r}\right) + H_{carboxysome} \end{aligned} \tag{A.28}$$

Here the concentration of CO_2 at the cell membrane,

$$C_{cytosol}(r = R_b) = \frac{k_m^C C_{out} - (\frac{a}{K_a} + k_m^C)C_{carboxysome}}{(\frac{a}{K_a} + k_m^C)G + \frac{D}{R_b^2}} G + C_{carboxysome} \tag{A.29}$$

A.0.4 Equations in carboxysome

In the carboxysome the equations are

$$\partial_t C = D\nabla^2 C + R_{CA} - R_{Rub} \tag{A.30}$$

$$\partial_t H = D\nabla^2 H - R_{CA}, \tag{A.31}$$

where the equation for the carbonic anhydrase reaction is

$$R_{CA}(H, C) = \frac{V_{ba}K_{ca}H - V_{ca}K_{ba}C}{K_{ba}K_{ca} + K_{ca}H + K_{ba}C} \tag{A.32}$$

Here V_{ba} and V_{ca} are the maximum rates of dehydration and hydration. K_{ba} and K_{ca} are the half maximum concentration rates for dehydration and hydration.

The equation for the RuBisCO reaction is

$$R_{Rub} = \frac{V_{max}C}{C + K_m} \tag{A.33}$$

$$K_m = K'_m(1 + \frac{O}{K_i}) \tag{A.34}$$

Here V_{max} is the maximum rate of carbon fixation by RuBisCO, and K_m is half maximum concentration rate, modified to include competitive binding with O_2, O.

We can use the solution in the cytosol to write a boundary condition at the carboxysome:

$$\begin{aligned}\frac{\partial C}{\partial r} &= -\frac{A_3}{r^2} \\ &= -\left(\frac{1}{R_c^2}\right)\frac{(\frac{a}{K_a} + k_m^C)C_{carboxysome} - k_m^C C_{out}}{(\frac{a}{K_a} + k_m^C)G + \frac{D}{R_b^2}}\end{aligned} \tag{A.35}$$

$$\begin{aligned}\frac{\partial H}{\partial r} &= -\frac{B_3}{r^2} \\ &= -\left(\frac{1}{R_c^2}\right)\frac{k_m^H H_{carboxysome} - (j_c + k_m^H)H_{out} - \frac{a}{K_a}C_{cytosol}(r = R_b)}{k_m^H G + \frac{D}{R_b^2}}\end{aligned} \tag{A.36}$$

A.0.5 RuBisCO negligible in setting up CO_2 concentration

When RuBisCO negligible we can find the solution in the carboxysome as a balance between the carbonic anhydrase dehydration reaction and either the hydration reaction or diffusion.

A.0.6 Carbonic anhydrase equilibrates carbon in carboxysome

If the carbonic anhydrase rate is faster than the diffusion rate then diffusion will be negligible and the solution in the carboxysome is set by $R_{CA} \approx 0$;

$$H_{carboxysome} \approx \frac{V_{ca}K_{ba}}{V_{ba}K_{ca}} C_{carboxysome}. \tag{A.37}$$

Another consequence of looking at equations (A.30) and (A.31) at steady state with $R_{Rub} \approx 0$ is that $\nabla^2(C+H) \approx 0$. Integrating once we get:

$$\begin{aligned} \frac{\partial(C+H)}{\partial r} &= \frac{a}{r^2} = 0 \\ \frac{\partial(C+H)}{\partial r}(r = R_c) &= 0 \end{aligned} \tag{A.38}$$

the constant a must be zero, or else we would get a divergent solution at $r = 0$. This is the same as mass conservation. Since the RuBisCO reaction is negligible, the total flux of inorganic carbon in and out of the carboxysome must balance. Using boundary conditions (A.35) and (A.36) in equation (A.38), we find a second equation for H and C.

$$\begin{aligned} &\frac{(\frac{a}{K_a} + k_m^C)C_{carboxysome} - k_m^C C_{out}}{(\frac{a}{K_a} + k_m^C)G + \frac{D}{R_b^2}} + \frac{k_m^H H_{carboxysome} - (j_c + k_m^H)H_{out}}{k_m^H G + \frac{D}{R_b^2}} \\ &\qquad - \frac{\frac{a}{K_a}\frac{k_m^C C_{out} - (\frac{a}{K_a} + k_m^C)C_{carboxysome}}{(\frac{a}{K_a} + k_m^C)G + \frac{D}{R_b^2}} G + \frac{a}{K_a} C_{carboxysome}}{k_m^H G + \frac{D}{R_b^2}} = 0 \end{aligned} \tag{A.39}$$

Using equation (A.66) we can find the CO_2 concentration in the carboxysome:

$$C_{carboxysome} = \frac{(j_c + k_m^H)H_{out}((k_m^C + \frac{a}{K_a})G + \frac{D}{R_b^2}) + k_m^C C_{out}((k_m^H + \frac{a}{K_a})G + \frac{D}{R_b^2})}{(k_m^C + \frac{a}{K_a})(1 + \frac{V_{ca}K_{ba}}{V_{ba}K_{ca}})k_m^H G + k_m^C(1 + \frac{k_m^H}{k_m^C}\frac{V_{ca}K_{ba}}{V_{ba}K_{ca}})\frac{D}{R_b^2}} \tag{A.40}$$

and the solution for H is set by (A.66).

Carbonic anhydrase saturated

It is possible for the hydration reaction to be negligible compared to diffusion when carbonic anhydrase becomes saturated. In this case $\nabla^2 H = \frac{Vba}{D}$ and $\nabla^2 C = -\frac{Vba}{D}$, implying

$$C = -\frac{V_{ba}}{6D} r^2 + A_1 \tag{A.41}$$

$$H = \frac{V_{ba}}{6D} r^2 + B_1. \tag{A.42}$$

applying boundary conditions (A.35) and (A.36) to these equations we find,

$$\begin{aligned} C_{carboxysome} =& \frac{V_{ba}}{3D} R_c^3 \left(G + \frac{D}{(\frac{a}{K_a} + k_m^C) R_b^2} \right) + \frac{V_{ba}}{6D} \left(R_c^2 - r^2 \right) \\ &+ \frac{k_m^C}{\frac{a}{K_a} + k_m^C} C_{out} \end{aligned} \tag{A.43}$$

$$\begin{aligned} H_{carboxysome} =& \frac{V_{ba}}{6D} (r^2 - R_c^2) - \frac{V_{ba}}{3D} R_c^3 \left(G + \frac{D}{k_m^H R_b^2} \right) \\ &+ \frac{(j_c + k_m^H)}{k_m^H} H_{out} + \frac{a}{k_m^H K_a} \left(\frac{k_m^C C_{out}}{(\frac{a}{K_a} + k_m^C) G + \frac{D}{R_b^2}} \right) \\ &+ \left(1 - \frac{(\frac{a}{K_a} + k_m^C) G}{(\frac{a}{K_a} + k_m^C) G + \frac{D}{R_b^2}} \right) \frac{a}{k_m^H K_a} C_{carboxysome} \end{aligned} \tag{A.44}$$

A.0.7 RuBisCO significant

If RuBisCO is significant then the approximation (A.38) doesn't hold. Instead we need to loosen the condition. Instead of the flux of $H + C$ out of the carboxysome being zero, it must be equal to the amount of CO_2 consumed in the carboxysome.

$$\int D\frac{\partial(C+H)}{\partial r}(r=R_c)dS_{carboxysome} = \int \frac{V_{max}C_{carboxysome}}{C_{carboxysome}+K_m}dV_{carboxysome} \tag{A.45}$$

$$4\pi R_c^2 D(-\frac{A_3}{R_c^2}-\frac{B_3}{R_c^2}) = \frac{4}{3}\pi R_c^3 \frac{V_{max}C_{carboxysome}}{C_{carboxysome}+K_m} \tag{A.46}$$

$$A_3+B_3 = -\frac{R_c^3}{3D}\frac{V_{max}C_{carboxysome}}{C_{carboxysome}+K_m} \tag{A.47}$$

with A_3 and B_3 defined as before:

$$A_3 = \frac{(\frac{a}{K_a}+k_m^C)C_{carboxysome}-k_m^C C_{out}}{(\frac{a}{K_a}+k_m^C)G+\frac{D}{R_b^2}} \tag{A.48}$$

$$B_3 = \frac{(k_m^H H_{carboxysome}-(j_c+k_m^H)H_{out}-\frac{a}{K_a}C_{cytosol}(r=R_b))}{k_m^H G+\frac{D}{R_b^2}} \tag{A.49}$$

We still use the fact that the carboxysome is small, and so diffusion equilibrates the concentration across the carboxysome very quickly. The equation for HCO_3^- therefore, still enforces the ratio $H_{carboxysome} \approx \frac{V_{ca}K_{ba}}{V_{ba}K_{ca}}C_{carboxysome}$.

If we define the following:

$$N = (j_c+k_m^H)H_{out}((k_m^C+\frac{a}{K_a})G+\frac{D}{R_b^2}) + k_m^C C_{out}((k_m^H+\frac{a}{K_a})G+\frac{D}{R_b^2}) \tag{A.50}$$

$$M = (k_m^C+\frac{a}{K_a})(1+\frac{V_{ca}K_{ba}}{V_{ba}K_{ca}})k_m^H G + k_m^C(1+\frac{k_m^H}{k_m^C}\frac{V_{ca}K_{ba}}{V_{ba}K_{ca}})\frac{D}{R_b^2} \tag{A.51}$$

$$P = ((\frac{a}{K_a}+k_m^C)G+\frac{D}{R_b^2})(k_m^H G+\frac{D}{R_b^2}) \tag{A.52}$$

then we can rewrite equation (A.47)

$$N - MC_{carboxysome} - \frac{R_c^3 V_{max} C_{carboxysome}}{3D(C_{carboxysome} + K_m)} P = 0 \tag{A.53}$$

$$C_{carboxysome}^2 + (K_m - \frac{N}{M} + \frac{R_c^3 V_{max} P}{3DM}) C_{carboxysome} - K_m \frac{N}{M} = 0 \tag{A.54}$$

$$\begin{aligned} C_{carboxysome} &= \frac{1}{2}(\frac{N}{M} - \frac{R_c^3 V_{max} P}{3DM} - K_m) \\ &\pm \frac{1}{2}\sqrt{(\frac{N}{M} - \frac{R_c^3 V_{max} P}{3DM} - K_m)^2 + 4\frac{N}{M} K_m} \end{aligned} \tag{A.55}$$

For comparison, when RuBisCO is not significant the solution, equation (A.40), can be written as

$$C_{carboxysome} = \frac{N}{M}. \tag{A.56}$$

When RuBisCO is significant but saturated, and the reaction is constant, we can make the approximation:

$$C_{carboxysome} = \frac{N}{M} - \frac{R_c^3 V_{max} P}{3MD}. \tag{A.57}$$

When RuBisCO is significant but unsaturated, and the reaction is linear in CO_2 concentration, we can make the approximation:

$$C_{carboxysome} = \frac{N}{M + \frac{R_c^3 V_{max} P}{3K_m D}}. \tag{A.58}$$

A.0.8 Reactions everywhere in cell

When RuBisCO and carbonic anhydrase are everywhere in the cell the equations previously used in the carboxysome apply everywhere:

$$\partial_t C = D\nabla^2 C + R_{CA} - R_{Rub} \tag{A.59}$$

$$\partial_t H = D\nabla^2 H - R_{CA}, \tag{A.60}$$

$$R_{CA}(H, C) = \frac{V_{ba} K_{ca} H - V_{ca} K_{ba} C}{K_{ba} K_{ca} + K_{ca} H + K_{ba} C} \tag{A.61}$$

$$R_{Rub} = \frac{V_{max} C}{C + K_m} \tag{A.62}$$

but now the only boundary condition is at the cell membrane;

$$D\frac{\partial C}{\partial r} = -\frac{a C_{cytosol}}{K_a + C_{cytosol}} + k_m^C \left(C_{out} - C_{cytosol}\right) \tag{A.63}$$

$$\begin{aligned} D\frac{\partial H}{\partial r} = j_c H_{out} + & \frac{a C_{cytosol}}{K_a + C_{cytosol}} \\ & + k_m^H \left(H_{out} - H_{cytosol}\right) \end{aligned} \tag{A.64}$$

Equations (A.59) and (A.60) can now be solved making the same approximations as before.

A.0.9 Carbonic anhydrase equilibrates carbon in cell

Using the analogous approximation to equation (A.38), set by boundary conditions (A.64) and (A.64),

$$\frac{\partial (C + H)}{\partial r}(r = R_b) = 0 \tag{A.65}$$

and

$$H_{cytosol} \approx \frac{V_{ca} K_{ba}}{V_{ba} K_{ca}} C_{cytosol}. \tag{A.66}$$

we find

$$\begin{aligned} & -\frac{a C_{cytosol}}{K_a + C_{cytosol}} + k_m^C \left(C_{out} - C_{cytosol}\right) \\ & + j_c H_{out} + \frac{a C_{cytosol}}{K_a + C_{cytosol}} + k_m^H \left(H_{out} - \frac{V_{ca} K_{ba}}{V_{ba} K_{ca}} C_{cytosol}\right) = 0 \end{aligned} \tag{A.67}$$

$$C_{cytosol} = \frac{k_m^C C_{out} + (j_c + k_m^H) H_{out}}{k_m^C (1 + \frac{k_m^H}{k_m^C} \frac{V_{ca} K_{ba}}{V_{ba} K_{ca}})} \tag{A.68}$$

Carbonic anhydrase saturated

When carbonic anhydrase concentration is low and saturated we have the same equations as before,

$$C = -\frac{V_{ba}}{6D}r^2 + A_1 \tag{A.69}$$

$$H = \frac{V_{ba}}{6D}r^2 + B_1. \tag{A.70}$$

and apply boundary conditions (A.63) and (A.64). We get:

$$C_{cytosol} = \frac{k_m^C C_{out}}{\frac{a}{K_a}+k_m^C} + V_{ba}\left(\frac{R_b}{3(\frac{a}{K_a}+k_m^C)} + \frac{R_b^2}{6D} - \frac{r^2}{6D}\right) \tag{A.71}$$

$$\begin{aligned} H_{cytosol} = {} & V_{ba}\left(\frac{r^2}{6D} - \frac{R_b^2}{6D} - \frac{R_b}{3k_m^H}\right) + \frac{j_c + k_m^H}{k_m^H}H_{out} \\ & + \frac{a}{K_a k_m^H}C_{cytosol}(r = R_b) \end{aligned} \tag{A.72}$$

A.0.10 RuBisCO significant

Following the same methodology as in section A.0.7, we write

$$\int D\frac{\partial(C+H)}{\partial r}|_{r=R_B} dS_{cell} = \int \frac{V_{max}C}{C+K_m}dV_{cell} \tag{A.73}$$

$$4\pi R_b^2 D\left(\frac{\partial C}{\partial r}|_{r=R_b} + \frac{\partial H}{\partial r}|_{r=R_b}\right) = \frac{4}{3}\pi R_b^3 \frac{V_{max}C}{C+K_m} \tag{A.74}$$

$$D\frac{\partial C}{\partial r}|_{r=R_b} + D\frac{\partial H}{\partial r}|_{r=R_b} = \frac{R_b}{3}\frac{V_{max}C}{C+K_m} \tag{A.75}$$

Where the two partial derivatives at $r = R_b$ are defined by boundary conditions (A.63) and (A.64).

We can define

$$N_2 = k_m^C C_{out} + (j_c + k_m^H)H_{out} \tag{A.76}$$

$$M_2 = k_m^C\left(1 + \frac{k_m^H}{k_m^C}\frac{V_{ca}K_{ba}}{V_{ba}K_{ca}}\right) \tag{A.77}$$

Note that N_2 and M_2 do not have the same dimensions as N and M defined previously. Using these definitions we can solve for the CO_2 concentration in the

cytosol.

$$N_2 - M_2 C - \frac{R_b}{3}\frac{V_{max} C}{C + K_m} = 0 \tag{A.78}$$

$$C_{cytosol}^2 + (K_m - \frac{N_2}{M_2} + \frac{R_b V_{max}}{3M_2}) C_{cytosol} - K_m \frac{N_2}{M_2} = 0 \tag{A.79}$$

$$\begin{aligned} C_{cytosol} = \frac{1}{2}\left(\frac{N_2}{M_2} - \frac{R_b V_{max}}{3M_2} - K_m\right) \\ + \frac{1}{2}\sqrt{(K_m - \frac{N_2}{M_2} + \frac{R_b V_{max}}{3M_2})^2 + \frac{4K_m N_2}{M_2}} \end{aligned} \tag{A.80}$$

The equation for CO_2 concentration assuming negligible RuBisCO activity, equation (A.68), can be rewritten:

$$C_{cytosol} = \frac{N_2}{M_2} \tag{A.81}$$

If RuBisCO is saturated then the concentration is described by:

$$C = \frac{N_2}{M_2} - \frac{R_b}{3} V_{max} \tag{A.82}$$

If RuBisCo is unsaturated:

$$C = \frac{N_2}{M_2 + \frac{R_b V_{max}}{3K_m}} \tag{A.83}$$

A.0.11 Reactions localized without carboxysome

We assume the region where the enzymes are located remains the same size. This could be accomplished by attaching the enzymes to a scaffold instead of incapsulating them.

When there is no carboxysome shell, the boundary condition at R_c changes to:

$$C_{cytosol} = C_{scaffold} \tag{A.84}$$

$$H_{cytosol} = H_{scaffold} \tag{A.85}$$

where the concentration in the cytosol is the same as before.

$$C_{cyto} = \frac{A_3}{r} + A_4 = A_3\left(\frac{1}{r} - \frac{1}{R_c}\right) + C_{scaffold} \tag{A.86}$$

$$H_{cyto} = \frac{B_3}{r} + B_4 = B_3\left(\frac{1}{r} - \frac{1}{R_c}\right) + H_{scaffold} \tag{A.87}$$

Plugging equations (A.86) and (A.87) into the following boundary conditions at the cell membrane.

$$D\frac{\partial C}{\partial r} = -\frac{aC_{cytosol}}{K_a + C_{cytosol}} + k_m^C\left(C_{out} - C_{cytosol}\right) \tag{A.88}$$

$$D\frac{\partial H}{\partial r} = j_c H_{out} + \frac{aC_{cytosol}}{K_a + C_{cytosol}} + k_m^H\left(H_{out} - H_{cytosol}\right) \tag{A.89}$$

The values of A_3 and B_3 are the same as before, but with a different definition of G.

$$A_3 = \frac{(\frac{a}{K_a} + k_m^C)C_{scaffold} - k_m^C C_{out}}{(\frac{a}{K_a} + k_m^C)G + \frac{D}{R_b^2}} \tag{A.90}$$

$$B_3 = \frac{(k_m^H H_{scaffold} - (j_c + k_m^H)H_{out} - \frac{a}{K_a}C_{cytosol}(r = R_b))}{k_m^H G + \frac{D}{R_b^2}} \tag{A.91}$$

$$G = \left(\frac{1}{R_c} - \frac{1}{R_b}\right) \tag{A.92}$$

$$C_{cytosol} = \frac{k_m^C C_{out} - (\frac{a}{K_a} + k_m^C)C_{scaffold}}{(\frac{a}{K_a} + k_m^C)G + \frac{D}{R_b^2}}\left(\frac{1}{R_C} - \frac{1}{r}\right) + C_{scaffold} \tag{A.93}$$

$$H_{cytosol} = \frac{(j_c + k_m^H)H_{out} + \frac{a}{K_a}C_{cytosol}(r = R_b) - k_m^H H_{scaffold}}{k_m^H G + \frac{D}{R_b^2}}\left(\frac{1}{R_C} - \frac{1}{r}\right) + H_{scaffold} \tag{A.94}$$

Here the concentration of CO_2 at the cell membrane,

$$C_{cytosol}(r = R_b) = \frac{k_m^C C_{out} - (\frac{a}{K_a} + k_m^C) C_{scaffold}}{(\frac{a}{K_a} + k_m^C) G + \frac{D}{R_b^2}} G + C_{scaffold} \tag{A.95}$$

The solution in the carboxysome is exactly what we have calculated before, in either the carbonic anhydrase equilibrating or saturated case, except with our new definition of G.

Colophon

This thesis was typeset using LaTeX, originally developed by Leslie Lamport and based on Donald Knuth's TeX. The body text is set in 11 point Arno Pro, designed by Robert Slimbach in the style of book types from the Aldine Press in Venice, and issued by Adobe in 2007. A template, which can be used to format a PhD thesis with this look and feel, has been released under the permissive mit (x11) license, and can be found online at github.com/suchow/ or from the author at suchow@post.harvard.edu.